Device

Article

Transition metal dichalcogenide solar cells for indoor energy harvesting

Graphical abstract

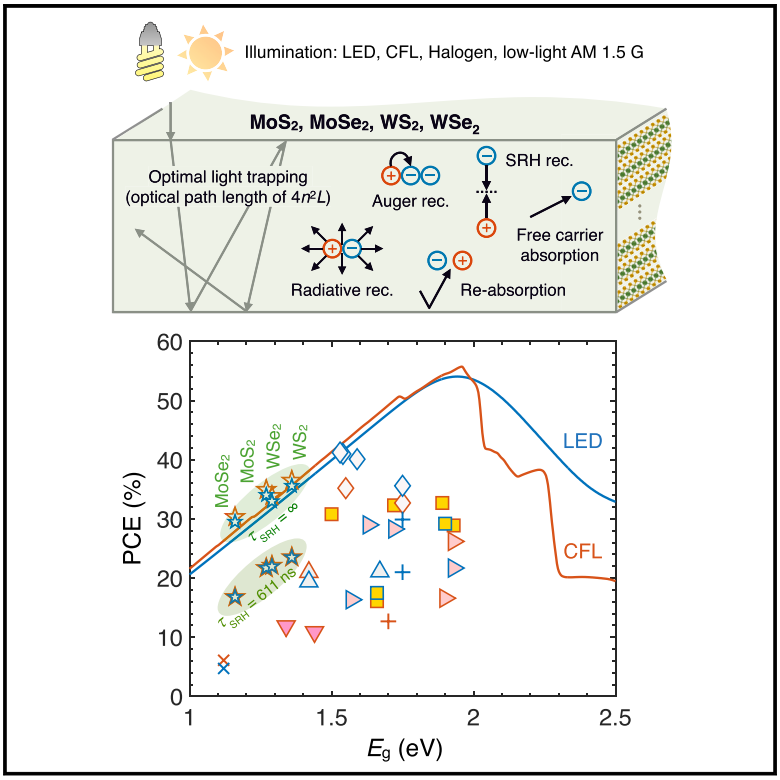

Highlights

- Transition metal dichalcogenides enable efficient indoor energy harvesting
- Realistic solar cell modeling under diverse indoor lighting conditions
- Potential to outperform commercial indoor photovoltaic technologies
- Indoor photovoltaics measurement standards ensure accurate performance assessments

Authors

Frederick U. Nitta, Koosha Nassiri Nazif, Eric Pop

Correspondence

epop@stanford.edu

In brief

Transition metal dichalcogenide (TMD) solar cells offer a promising solution for powering Internet of Things (IoT) devices in indoor environments. This realistic modeling study demonstrates that TMD solar cells, once optimized, could achieve superior power conversion efficiencies compared to commercial indoor photovoltaic technologies under various lighting conditions. By leveraging their high absorption coefficients and layered van der Waals structure, TMD solar cells could transform how indoor light energy is harvested, enabling more reliable and sustainable power sources for the rapidly growing IoT ecosystem.

Understand
Early stage research on device properties, design, and physics

Nitta et al., 2025, Device *3*, 100723
July 18, 2025
https://doi.org/10.1016/j.device.2025.100723

CellPress

Device

CellPress
OPEN ACCESS

Article

Transition metal dichalcogenide solar cells for indoor energy harvesting

Frederick U. Nitta,[1,2] Koosha Nassiri Nazif,[1] and Eric Pop[1,2,3,4,*]
[1]Department of Electrical Engineering, Stanford University, Stanford, CA 94305, USA
[2]Department of Materials Science and Engineering, Stanford University, Stanford, CA 94305, USA
[3]Department of Applied Physics, Stanford University, Stanford, CA 94305, USA
[4]Lead contact
*Correspondence: epop@stanford.edu
https://doi.org/10.1016/j.device.2025.100723

THE BIGGER PICTURE As the Internet of Things (IoT) expands, the demand for efficient and durable energy sources to power indoor devices becomes increasingly critical. Solar cells based on transition metal dichalcogenides (TMDs) offer a promising solution due to their desirable optoelectronic properties. This research highlights the potential of TMD solar cells to outperform commercial indoor photovoltaics and to power IoT sensors and communication protocols in everyday environments like homes, offices, and retail spaces. To fully realize the potential of TMD solar cells, future efforts should focus on improving material quality to reduce defects, which limit efficiency, and to optimize optical and electrical designs to maximize light absorption and carrier extraction. Such advances could establish TMD-based solar cells as a key component of sustainable energy solutions for the growing IoT ecosystem.

SUMMARY

As the Internet of Things (IoT) expands, more IoT devices will need to be powered by efficient and durable energy harvesters, both indoors and outdoors. Transition metal dichalcogenides (TMDs), such as MoS_2, $MoSe_2$, WS_2, and WSe_2, are promising materials for indoor photovoltaics (PV) due to their high absorption coefficients and self-passivated surfaces. Here, we assess the performance of single-junction multilayer ($\geq$5 nm thick) TMD solar cells under various indoor lighting conditions with a realistic detailed balance model including material-specific optical absorption as well as radiative, Auger, and defect-assisted Shockley-Read-Hall recombination. TMD solar cells could achieve up to 36.5%, 35.6%, 11.2%, and 27.6% power conversion efficiency under fluorescent, light-emitting diode (LED), halogen, and low-light AM 1.5 G lighting, respectively, at 500 lux. Based on this, TMD solar cells could outperform commercial indoor PV technologies (e.g., amorphous silicon and dye-sensitized solar cells), suggesting their viability for future IoT energy solutions.

INTRODUCTION

As the Internet of Things (IoT) expands, the need for reliable energy sources to power IoT devices becomes increasingly vital, especially within indoor environments. Indoor photovoltaics (PV) offer a sustainable solution, addressing the energy requirements for the vast network of sensors and devices that will form the backbone of data-driven sectors such as healthcare, manufacturing, infrastructure, and energy. It is anticipated that billions of wireless sensors will be deployed in the next decade, with a substantial number located indoors to facilitate continuous data acquisition and system optimization.[1,2]

While several indoor PV technologies, such as amorphous silicon (a-Si),[3] dye-sensitized solar cells (DSSCs),[4,5] organic PV,[6,7] and perovskite solar cells,[8–10] have been explored, each presents some challenges in terms of efficiency, stability, and production scalability.[11–18] Among emerging materials and technologies for indoor PV solutions, transition metal dichalcogenides (TMDs) are attracting attention due to their high absorption coefficients, near-ideal band gaps, and self-passivated surfaces.[19,20] Models show that ultrathin TMD solar cells (~50 nm) can achieve 25% power conversion efficiency outdoors—under the AM 1.5 G spectrum—upon design optimization even with existing material quality. This corresponds to 10× higher specific power compared with that of existing incumbent solar cell technologies.[21] Although similarly high performance is expected from TMD solar cells indoors, there are no prior studies of the performance of TMD solar cells that quantify the power output of TMD solar cells indoors.

In this work, we provide thickness-dependent efficiency limits for single-junction solar cells made of multilayer ($\geq$5-nm-thick) MoS_2, $MoSe_2$, WS_2, and WSe_2 solar cells at different material qualities and under various indoor lighting conditions. We use a realistic

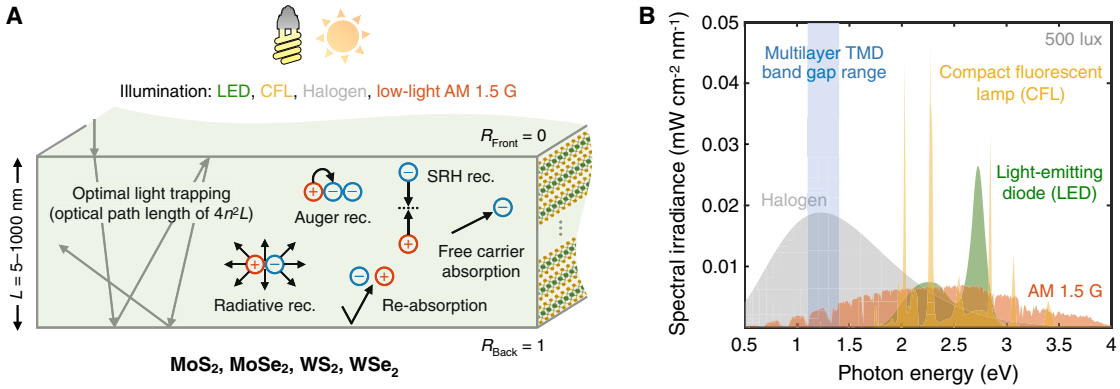

Figure 1. Indoor TMD photovoltaics

(A) Modeling setup showing the configuration of a multilayer transition metal dichalcogenide (TMD) solar cell with various illumination sources. Optimal light trapping with an optical path length of $4n^2L$ is considered, and various recombination mechanisms are included. Anti-reflection coatings and a perfect back reflector are used to enhance light absorption and minimize reflective losses. *R*, reflection; *L*, TMD film thickness; *n*, refractive index; SRH rec., Shockley-Read-Hall recombination.

(B) Various indoor light spectra[23] used in this study. The band-gap range of multilayer TMDs is indicated by the blue-shaded region. All spectra are normalized at 500 lux (retail store conditions).

detailed balance model that has not been applied previously to indoor PV technologies, incorporating measured optical properties as well as radiative, Auger, and Shockley-Read-Hall (SRH) recombination. The performance of these solar cells is analyzed under various indoor light sources, including compact fluorescent lamp (CFL), light-emitting diode (LED), halogen, and low-intensity AM 1.5 G lighting, all adjusted to the illuminance levels typical in common indoor locations ranging from parking garages (50 lux) to retail stores (500 lux). We find that TMD solar cells could achieve high power conversion efficiencies of up to 36.5% under CFL, 35.6% under LED, 11.2% under halogen, and 27.6% under low-light AM 1.5 G lighting. This indicates that TMDs offer an improvement over existing indoor PV technologies, potentially transforming energy solutions for indoor IoT applications.

RESULTS

Modeling setup

Our modeling approach, detailed in our previous work[21] and in Note S1, extends beyond the Tiedje-Yablonovitch limit[22] to investigate the impact of material quality on solar cell performance. It incorporates defect-assisted SRH recombination to establish efficiency limits for single-junction, multilayer TMD solar cells with film thicknesses of 5 nm or more as a function of material quality. It considers enhanced absorption via a mean path length of $4n^2L$ (with *n* representing the refractive index) and photogenerated excitons that immediately dissociate into free charge carriers (Figure 1A). Unlike simplified models that assume step-function absorption or radiative recombination alone, our detailed balance model uses measured optical absorption data and accounts for non-radiative loss mechanisms, enabling more accurate predictions of achievable efficiency limits across varying material qualities. By focusing on fundamental properties, this model ensures that the derived efficiency limits remain broadly applicable regardless of the device design and configuration.

We examined the efficiency limits of TMD solar cells under four indoor spectra[23]: CFL, also known as energy-saving lamp, incandescent halogen, LED, and low-light AM 1.5 G. These spectra are shown in Figure 1B. The halogen spectrum was extended using the blackbody radiation formula (Note S2; Figure S1) to match the halogen lamp's emission characteristics. Normalization of these spectra to typical indoor lighting scenarios was achieved by matching the lux levels defined in the Illuminating Engineering Society (IES) Lighting Handbook.[24] These scenarios range from the lower intensity of a parking garage at 50 lux and a warehouse at 150 lux to brighter conditions of an office at 400 lux and a retail store at 500 lux.

Figure 1B shows the normalization of these spectra for a retail setting (500 lux) as an example. The lux illumination was calculated by calibrating the spectral power distribution with the Commission Internationale de l'Eclairage photopic luminosity function. Although lux values are based on the human-visible range, the input power calculations consider the full spectra of light wavelengths, which are needed to determine the power conversion efficiency (the ratio of output power to input power). The input power densities for the four indoor spectra at the lux levels considered are listed in Table S1. This calibration process is in line with methodologies applied to the AM 1.5 G spectrum in a previous study.[25]

Recommendation for indoor PV measurement standards

To ensure accurate performance assessments of indoor PV devices, future standards should consider normalizing spectral power distributions to specific lux conditions, as described here, while also incorporating protocols for measuring device performance across varying spectra and intensities. These standards could include a set of reference light sources, such as CFL, LED, halogen, and AM 1.5 G at defined lux levels to ensure consistency and reproducibility. The lux levels used in this study—50 lux (parking garage), 150 lux (warehouse), 400 lux (office), and 500 lux (retail store)—are drawn from the IES Lighting Handbook[24] to reflect realistic indoor lighting scenarios. These choices ensure that performance comparisons are based on practical

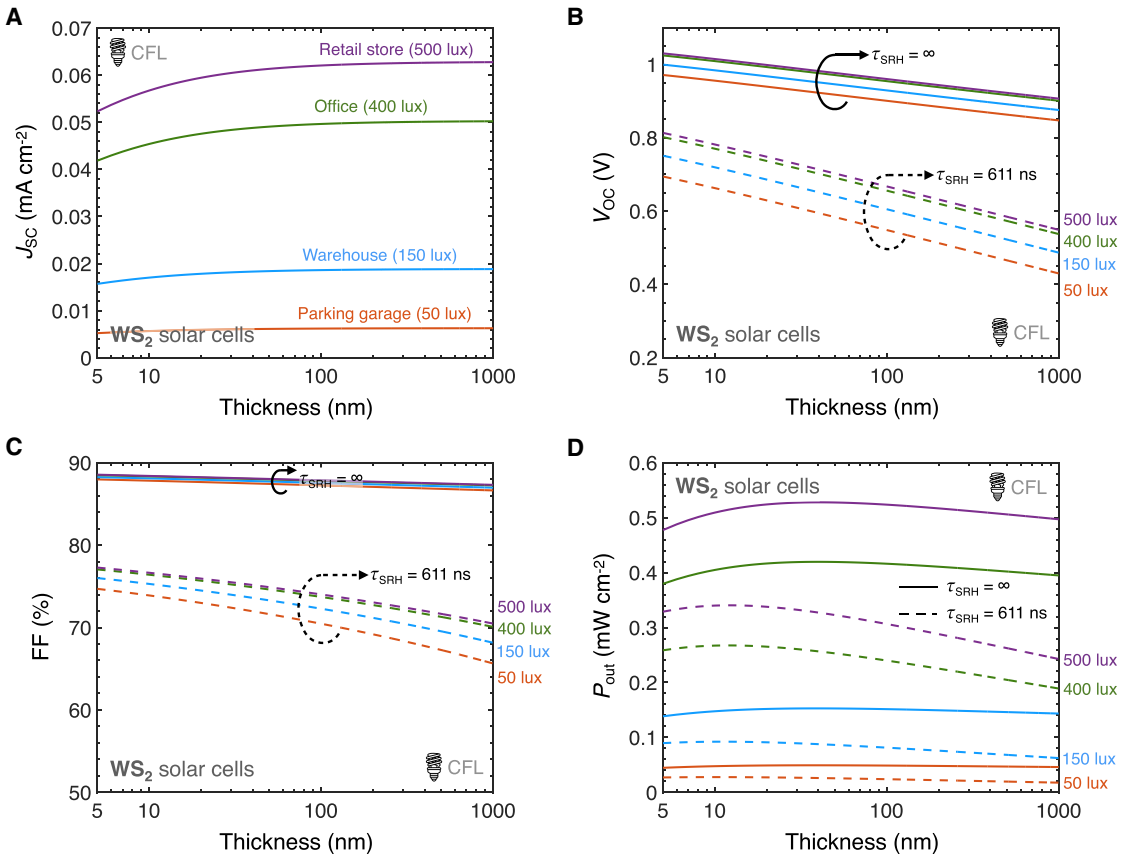

Figure 2. WS_2 solar cells with compact fluorescent lamp (CFL) illumination

Shown are (A) short-circuit current density (J_{SC}), (B) open-circuit voltage (V_{OC}), (C) fill factor (FF), and (D) output power (P_{out}), all as a function of WS_2 film thickness, at 300 K. Solid lines are in the limit defect-free material (no SRH recombination) and dashed lines with τ_{SRH} = 611 ns. Four CFL illumination intensities correspond to the four colors as labeled (e.g., purple dashed and solid lines are at 500 lux). Note that J_{SC} is not affected by material quality (τ_{SRH}) due to the low carrier density at zero bias.

conditions where indoor solar cells are expected to operate, providing a clear benchmark for researchers and developers.

The following sections delve into a detailed analysis of the results, including short-circuit current density, open-circuit voltage, fill factor, output power, and power conversion efficiency of single-junction TMD (MoS_2, $MoSe_2$, WS_2, and WSe_2) solar cells for each considered light source (CFL, LED, halogen, and AM 1.5 G) at various illuminance levels typical in common indoor locations, ranging from parking garages (50 lux) to retail stores (500 lux).

CFL

To illustrate the CFL estimates for one of the TMDs (here, WS_2), Figure 2 shows the calculated short-circuit current density (J_{SC}), open-circuit voltage (V_{OC}), fill factor (FF), and output power (P_{out}) under CFL lighting as a function of WS_2 film thickness and CFL illumination intensity. For this study, our choice of SRH lifetime (τ_{SRH}) of 611 ns is based on the maximum value reported to date for unpassivated multilayer WS_2[26]; our expectation is that, as material quality continues to improve (and/or TMD surfaces are passivated), the lifetimes for WS_2 and other TMDs will increase beyond this figure. In comparison, an infinite τ_{SRH} represents an idealized scenario (the Tiedje-Yablonovitch limit[22]), which points to the maximum achievable V_{OC} (and efficiency) in the absence of defect-assisted SRH recombination. Because the τ_{SRH} is inversely proportional to defect density, higher-quality materials with fewer defects will exhibit longer lifetimes, enabling reduced non-radiative recombination and improved device performance.[27]

The J_{SC} in Figure 2A has minimal variation with increasing film thickness at low light intensities, such as those in parking garages (50 lux) or warehouses (150 lux). However, at the higher intensities in office (400 lux) and retail (500 lux) environments, the enhanced absorption of lower-energy photons by thicker WS_2 films leads to a modest rise[27] in J_{SC}. Figure 2B shows that the V_{OC} similarly increases with light intensity but decreases with thicker films, as predicted by analytical models.[27] This occurs because the longer optical path in thicker films[22] causes better "light trapping," which enhances absorption of lower-energy photons and shifts the effective absorption threshold to lower energy[21] and lower V_{OC}. The scaling of V_{OC} with light intensity stems from the logarithmic relationship[27] between V_{OC} and photocurrent. The FF is influenced by both V_{OC} and material quality.[27] For a finite τ_{SRH} of 611 ns, both V_{OC} and FF (Figure 2C) are lower, and the FF shows

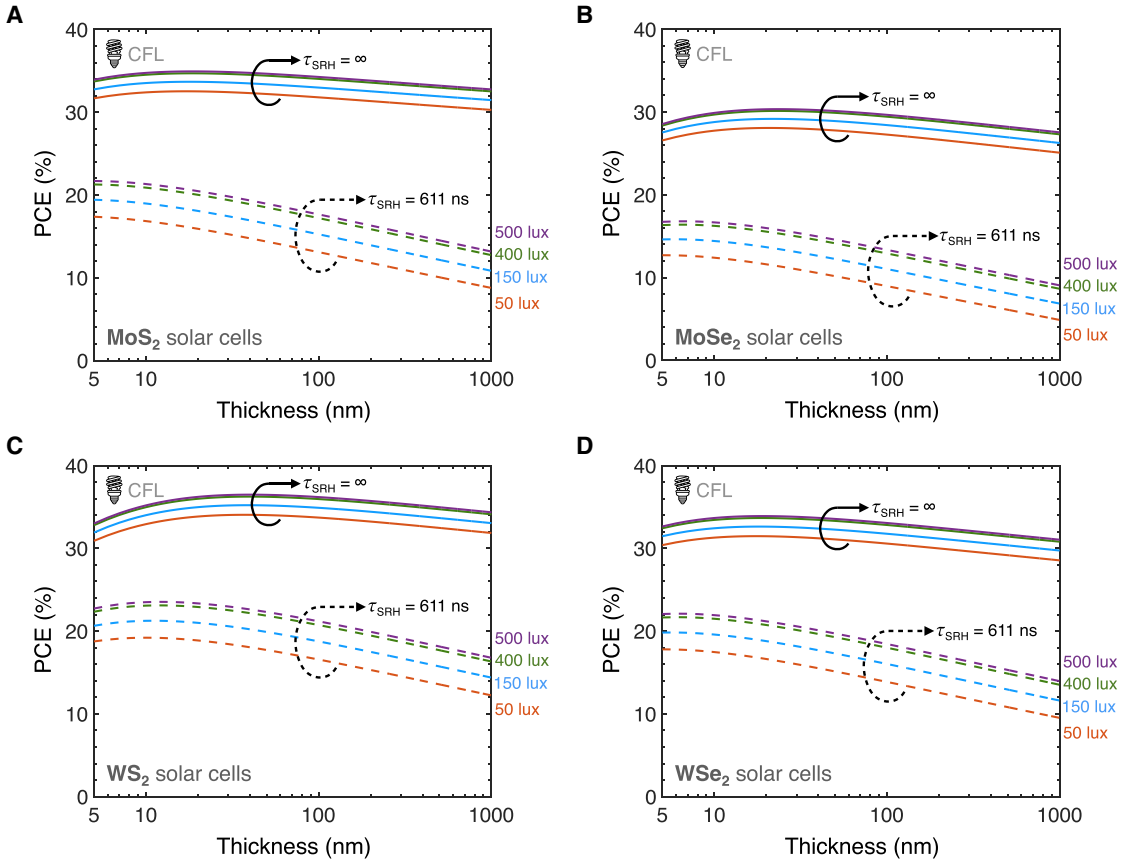

Figure 3. Power conversion efficiency (PCE) of thin-film TMD solar cells under ompact fluorescent lamp (CFL) illumination

Shown are the PCEs of (A) MoS_2, (B) $MoSe_2$, (C) WS_2, and (D) WSe_2 solar cells as a function of TMD film thickness, material quality (τ_{SRH}), and CFL illumination intensity at 300 K. Solid lines are in the limit defect-free material (no SRH recombination) and dashed lines with $\tau_{SRH} = 611$ ns. Illumination intensities correspond to the four colors as labeled (e.g., purple dashed and solid lines are at 500 lux). τ_{SRH}, SRH lifetime.

a stronger dependence on light intensity due to the greater relative impact of recombination at defect sites under lower light conditions. Although recombination is reduced at lower light intensities, the fewer available carriers make recombination losses more detrimental to the FF, particularly in thicker films with more defects. The dependency of FF on V_{OC} further explains its reduction with increasing film thickness.[28] Lastly, reflecting trends from the other parameters, P_{out} (Figure 2D) displays a weak inverted U shape as a function of film thickness. The P_{out} peaks at intermediate thicknesses, where the increase in J_{SC}, particularly at the higher light intensities, compensates for losses in V_{OC} and FF.

The power conversion efficiency (PCE) for MoS_2, $MoSe_2$, WS_2, and WSe_2 solar cells as a function of TMD film thickness, τ_{SRH}, and CFL illumination intensity is shown in Figure 3. PCE is the ratio of the P_{out} to the input power (P_{in}), and it characterizes the efficiency with which the solar cells convert the absorbed light into electrical power.[27] Because the P_{out} of solar cells is the product of J_{SC}, V_{OC}, and FF, these trends are explained by the J_{SC}, V_{OC}, and FF trends in Figures S2–S4, respectively. As observed, the P_{out} curves for all four TMDs (Figure S5) exhibit an inverted U-shape, which also defines the PCE curve due to the competing influences of J_{SC}, V_{OC}, and FF on the P_{out}. As the TMD film thickness increases, the J_{SC} improves due to better light absorption, but both V_{OC} and FF decrease, which is more pronounced for the finite τ_{SRH} of 611 ns. This competition leads to the same trends observed for PCE as for P_{out} with thickness.

The trends in J_{SC}, V_{OC}, and FF under CFL illumination are shaped by the narrower spectral distribution of the CFL light source, which peaks at higher photon energies (~2–3.5 eV). At greater thicknesses, J_{SC} begins to plateau as the absorption of photons within this energy range becomes nearly complete, limiting further gains in photocurrent. However, increasing recombination losses at higher thicknesses cause declines in V_{OC} and FF, which eventually outweigh the modest improvements in J_{SC}. This balance explains the higher PCE in thinner layers (Figure 3); TMDs achieve high PCEs even at tens of nanometers of thickness, far below the thickness required for conventional silicon solar cell absorbers (~100 μm).[29]

For lower light intensities, even though the P_{out} may not exhibit a distinct peak (Figure S5), the division by a relatively smaller P_{in} accentuates the peak in PCE (Figure 3). For an infinite τ_{SRH} where non-radiative recombination is excluded, the degradation in PCE with increased thickness is less severe, illustrating the critical role of material quality in TMD solar cell performance.

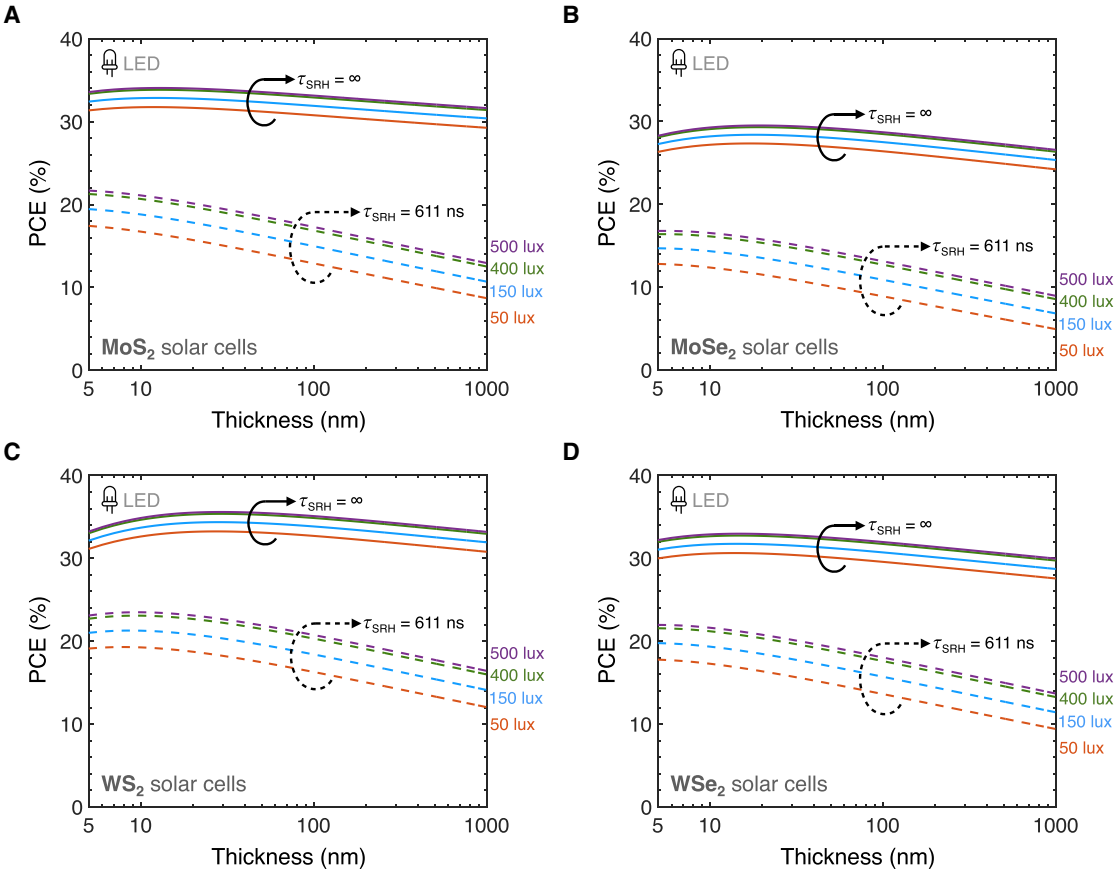

Figure 4. Power conversion efficiency (PCE) of thin-film TMD solar cells under light-emitting diode (LED) illumination

Shown are the PCEs of (A) MoS_2, (B) $MoSe_2$, (C) WS_2, and (D) WSe_2 solar cells as a function of TMD film thickness, material quality (τ_{SRH}), and LED illumination intensity at 300 K. Solid lines are in the limit defect-free material (no SRH recombination) and dashed lines with $\tau_{SRH} = 611$ ns. Illumination intensities correspond to the four colors as labeled (e.g., purple dashed and solid lines are at 500 lux).

Conversely, in the presence of SRH recombination, due to the steeper decline in V_{OC} and FF with thickness (Figures S3 and S4), the PCE exhibits a peak shift toward smaller thicknesses as well as a more significant drop-off with thickness.

With today's material quality ($\tau_{SRH} \approx 611$ ns), TMD solar cells can achieve up to 23.5% PCE under CFL illumination. The efficiency limits at current material quality could be achieved through careful optimization of the solar cell's optical and electrical designs. Optimal optical designs can include advanced light management techniques, such as the integration of back reflectors or scattering layers,[30] to maximize photon absorption in nanoscale films, while electrical performance can be enhanced by introducing doping[31,32] and carrier-selective contacts[33,34] to maximize carrier extraction. As material quality improves toward an infinite τ_{SRH}, PCEs as high as 36.5% become achievable, underscoring that better material quality directly correlates with enhanced performance.

LED lamp

We now examine the PCE for all four TMD solar cells with LED illumination as a function of TMD film thickness, LED illumination intensity, and τ_{SRH}, as shown in Figure 4. Thicker films initially enhance J_{SC} (Figure S6), contributing to an increase in PCE due to improved light absorption capabilities. This increase in PCE is, however, countered by decreases in V_{OC} (Figure S7) and FF (Figure S8), particularly where the τ_{SRH} is finite. The P_{out} trends (Figure S9) and, thus, the PCE trends, similar to those under CFL illumination, show that there is an optimal thickness where benefits in J_{SC} are maximized before being outweighed by losses in V_{OC} and FF. With infinite τ_{SRH}, the drop in PCE with increased thickness is not as pronounced thanks to the higher material quality. At a finite τ_{SRH}, a sharper peak and a more noticeable decline in PCE with additional thickness are observed. These trends suggest that enhancing material quality can significantly improve the PCE of TMD-based solar cells under LED lighting.

The PCE is highest at similar thicknesses as observed under CFL illumination (tens of nanometers) due to the LED spectrum's similarly narrower spectral distribution, with peaks near ~2.25 and ~2.73 eV. Unlike the broader spectra of halogen or low-light AM 1.5 G, the LED spectrum provides fewer low-energy photons (below ~2 eV) to benefit from additional absorption in thicker films. As a result, the enhancement in J_{SC} with increasing thickness diminishes more quickly, while recombination losses at larger thicknesses drive the declines in V_{OC} and FF, leading to

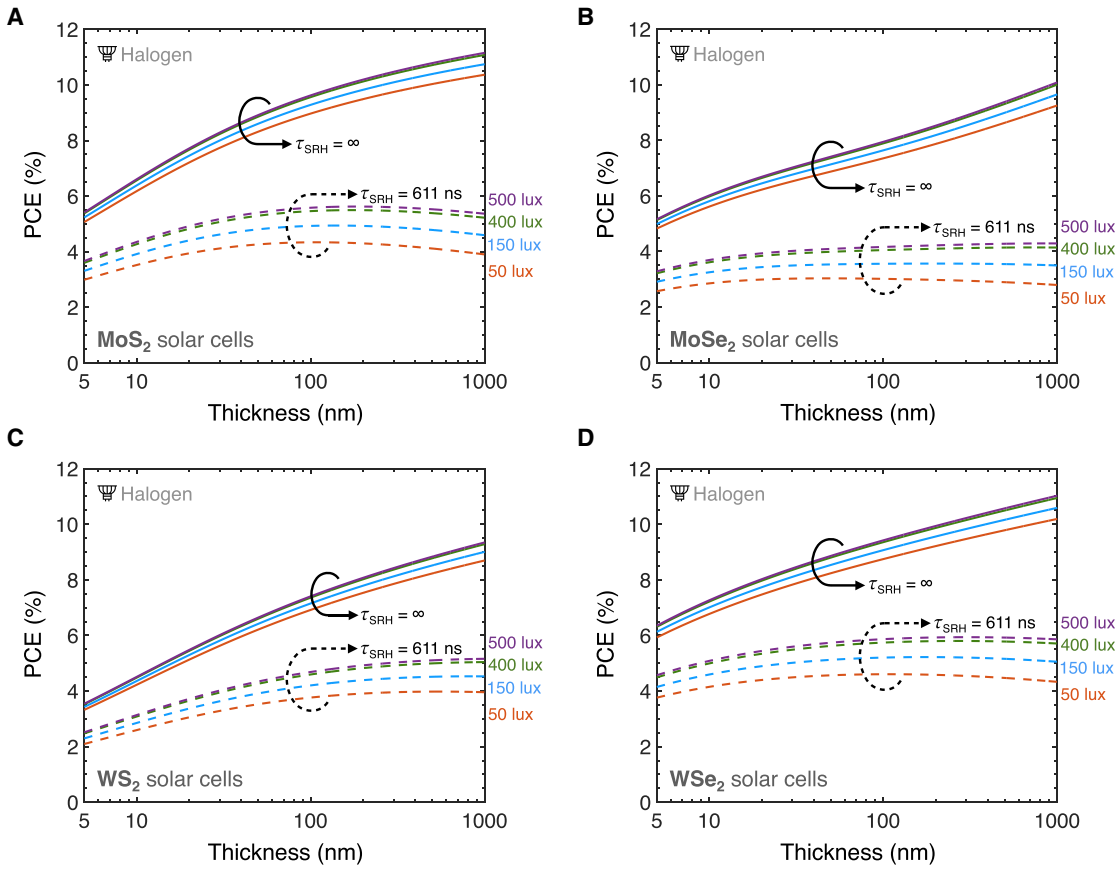

Figure 5. Power conversion efficiency (PCE) of thin-film TMD solar cells under halogen illumination

Shown are the PCEs of (A) MoS_2, (B) $MoSe_2$, (C) WS_2, and (D) WSe_2 solar cells as a function of TMD film thickness, material quality (τ_{SRH}), and halogen illumination intensity at 300 K. Solid lines are in the limit defect-free material (no SRH recombination) and dashed lines with $\tau_{SRH} = 611$ ns. Illumination intensities correspond to the four colors as labeled (e.g., purple dashed and solid lines are at 500 lux).

PCE peaks at ultrathin thicknesses. The PCEs under LED illumination are also comparable to those under CFL illumination because both spectra have similar P_{in} densities (Table S1) and are dominated by higher-energy (above band gap) photons that are efficiently absorbed by the TMD films.

With today's material quality ($\tau_{SRH} \approx 611$ ns), TMD solar cells can achieve up to 23.5% PCE under LED illumination. As material quality advances toward an infinite τ_{SRH}, there is potential to reach PCEs as high as 35.6%. These enhancements in PCE can be realistically attained by optimizing the optical and electrical designs of the TMD solar cells and leveraging improvements in material quality.

Halogen lamp

Examining the four TMD solar cells with halogen illumination, Figure 5 displays their estimated PCE as a function of TMD film thickness, τ_{SRH}, and halogen illumination intensity. The trends in J_{SC} (Figure S10), V_{OC} (Figure S11), and FF (Figure S12) inform the trends in P_{out} (Figure S13) and, thus, PCE. Notably, for an infinite τ_{SRH}, we observe a continuous increase in PCE across all materials, suggesting the benefit of improvements in J_{SC} with thicker films outweighing losses in V_{OC} and FF. However, the PCE under halogen illumination is overall lower than the PCE under CFL or LED illumination (Figures 3 and 4) due to the halogen spectrum having more low-energy photons, below the TMD band gaps (Figure 1B). For a finite τ_{SRH} of 611 ns, MoS_2 (Figure 5A) and WSe_2 (Figure 5D) exhibit discernible PCE peaks, indicating an optimal thickness range for maximum PCE. In contrast, the PCE of $MoSe_2$ (Figure 5B) is almost independent of film thickness, which points to its less dramatic balance between J_{SC} gains and V_{OC} and FF losses. The PCE of WS_2 (Figure 5C) shows a monotonic increase with film thickness, which is more pronounced at the higher illumination intensities. This demonstrates how the material's absorption spectrum and the illumination intensity affect PCE.

The halogen spectrum is significantly broader than those of CFL and LED lighting, extending to lower photon energies (below ~1.5 eV) that can still be absorbed by thicker TMD films. These additional low-energy photons enable J_{SC} to continue improving with increasing thickness. At a finite τ_{SRH}, the recombination losses in V_{OC} and FF become more pronounced with increasing thickness, eventually leading to PCE peaks at significantly larger thicknesses (hundreds of nanometers) compared to CFL and LED illumination.

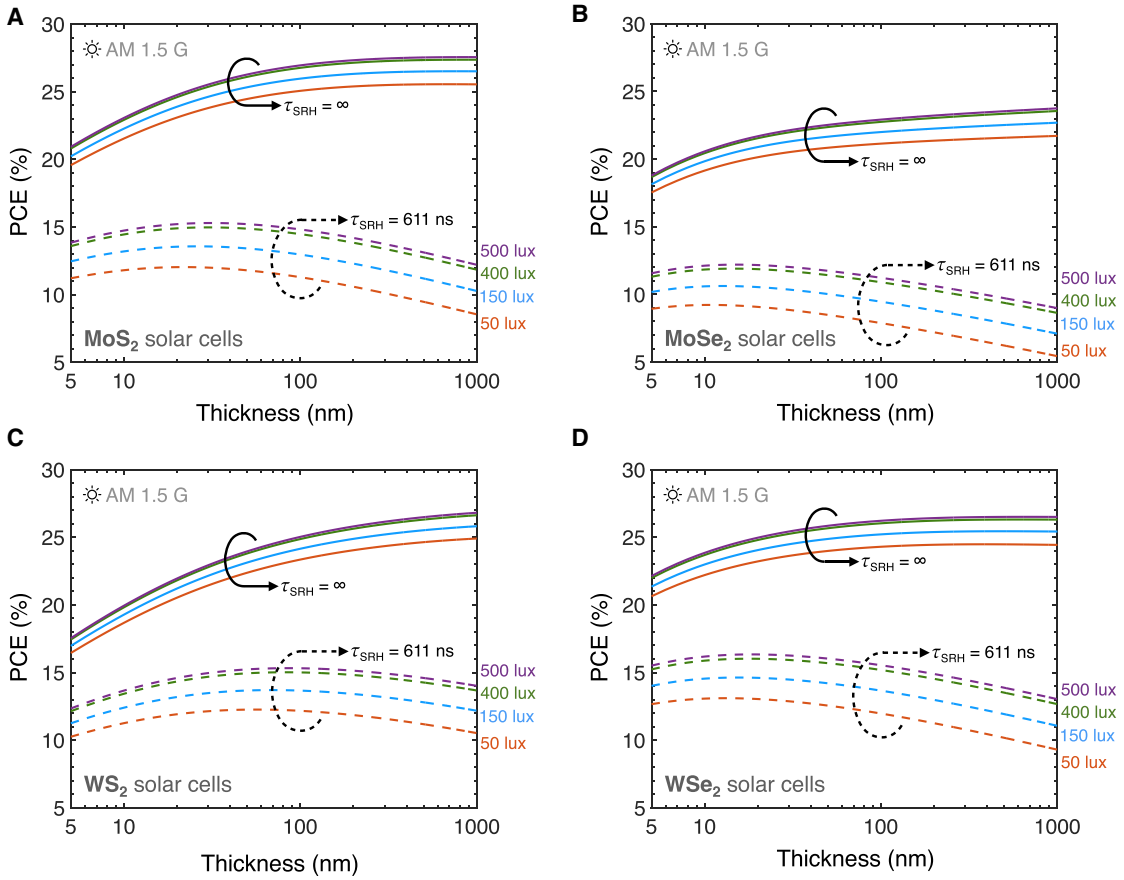

Figure 6. Power conversion efficiency (PCE) of thin-film TMD solar cells under AM 1.5 G illumination

Shown are the PCEs of (A) MoS_2, (B) $MoSe_2$, (C) WS_2, and (D) WSe_2 solar cells as a function of TMD film thickness, material quality (τ_{SRH}), and AM 1.5 G illumination intensity at 300 K. Solid lines are in the limit defect-free material (no SRH recombination) and dashed lines with τ_{SRH} = 611 ns. Illumination intensities correspond to the four colors as labeled (e.g., purple dashed and solid lines are at 500 lux).

With today's material quality, at $\tau_{SRH} \approx 611$ ns, these TMD solar cells can achieve up to 5.9% PCE under halogen illumination. As material quality advances toward an infinite τ_{SRH}, PCEs up to 11.2% may be reachable in the thickest MoS_2 and WSe_2 films under halogen illumination.

Low-light AM 1.5 G

The PCEs for MoS_2, $MoSe_2$, WS_2, and WSe_2 solar cells as a function of TMD film thickness, τ_{SRH}, and AM 1.5 G illumination intensity are shown in Figure 6. Similar to observations under halogen illumination, for an infinite τ_{SRH}, the PCEs consistently increase with film thickness for all materials, indicating that the positive effects of increased J_{SC} (Figure S14) with thickness outweigh the negative impacts on V_{OC} (Figure S15) and FF (Figure S16). Similar trends are seen for P_{out} (Figure S17) with an infinite τ_{SRH}. The PCE values under low-light AM 1.5 G are higher than for halogen illumination but lower than for CFL/LED illumination, a trend consistent with the availability of low-energy photons among these sources.

However, for a finite τ_{SRH} of 611 ns, P_{out} and PCE curves exhibit distinct peaks for all materials, similar to trends seen with CFL and LED illumination. These peaks highlight the interplay between J_{SC}, V_{OC}, and FF in determining the efficiency of light absorption and conversion to electrical power. Increasing film thickness enhances J_{SC} due to improved light absorption, but this benefit is counterbalanced by more substantial declines in both V_{OC} and FF in the thicker films.

For low-light AM 1.5 G, the PCE peaks occur at intermediate thicknesses compared to those under CFL/LED and halogen illumination. This is due to the broader spectral distribution of AM 1.5 G light, which includes more low-energy photons than CFL/LED but fewer than halogen light. These additional low-energy photons enable continued improvement in J_{SC} with increasing thickness, although at a slower rate than halogen, while recombination losses in V_{OC} and FF still dominate at greater thicknesses. As a result, the peaks for PCE occur at thicknesses that balance the incremental gains in J_{SC} with the more moderate losses in V_{OC} and FF, differentiating AM 1.5 G from the other light sources.

With today's material quality ($\tau_{SRH} \approx 611$ ns), TMD solar cells achieve a PCE of up to 16.3% under AM 1.5 G illumination at 500 lux (i.e., typical retail store lighting). As material quality

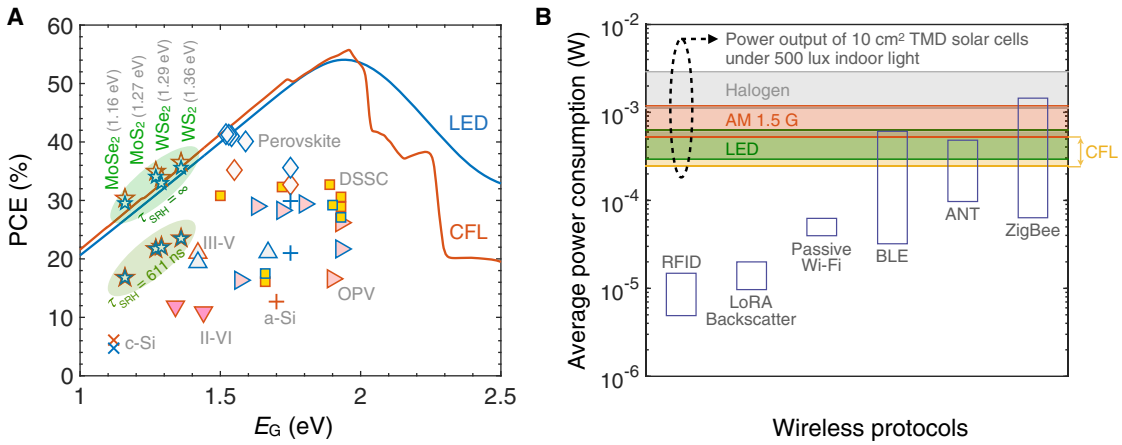

Figure 7. Comparison of TMD solar cells with other indoor PV technologies and IoT wireless protocols

(A) Maximum power conversion efficiency (PCE) vs. band gap (E_g) for indoor PV devices to date; symbols with an orange (blue) border mark measurements under CFL (LED) illumination. Orange (blue) lines mark the Shockley-Queisser limit at 500 lux with a CFL (LED) illumination spectrum. Indoor PV PCEs are at approximately 500- to 1,000-lux illumination; see Table S2 for more details and references. TMD estimates from this work (stars) are at 500 lux illumination at τ_{SRH} of 611 ns and infinite τ_{SRH} for both CFL and LED.

(B) Comparison of average power consumption of various wireless protocols[2,35,36] with P_{out} of 10 cm^2 TMD solar cells under various indoor lighting conditions at 500 lux. This highlights the ability of TMD solar cells to efficiently power IoT devices across multiple indoor settings, underscoring their potential to support the sustainable expansion of IoT networks. RFID (Radio Frequency Identification), LoRA (Long Range) backscatter, BLE (Bluetooth Low Energy), and ANT (Adaptive Network Topology).

progresses toward an infinite τ_{SRH}, the PCE could increase to as much as 27.6%. These efficiency limits are attainable by refining the optical and electrical designs of these ultrathin TMD solar cells.

DISCUSSION

Benchmarking and projections

Figure 7A benchmarks the PCE of TMD solar cells in this work against incumbent and emerging indoor PV technologies under CFL and LED illumination at ~500 lux, as detailed in Table S2. Shockley-Queisser efficiency limits considering a CFL spectrum and an LED spectrum at 500 lux are included for reference (Figure 7A, solid lines). For CFL illumination, TMD solar cells achieve a PCE of up to 23.5% at a τ_{SRH} of 611 ns and 36.5% in the absence of SRH recombination, both for WS_2. Under LED illumination, these PCEs are slightly lower at 23.5% and 35.6%, respectively. For an infinite τ_{SRH}, TMD solar cell PCEs above the Shockley-Queisser model are due to our incorporation of measured optical absorption spectra, which show that the absorption threshold of TMDs shifts to higher photon energies in thinner films, effectively increasing the band gap. This results in higher V_{OC} than predicted by the Shockley-Queisser model and, thus, higher FF, leading to higher overall PCEs.[21]

Our estimated TMD solar cell PCEs, achievable with optimized optical and electronic designs, are comparable to those of existing indoor PV technologies, such as DSSCs and organic PV, under similar conditions. Even at a τ_{SRH} of 611 ns, which corresponds to existing TMD material quality,[26] TMD solar cells are competitive with a-Si, III–V, II–VI, and crystalline Si technologies. Notably, the PCEs of TMD solar cells with infinite τ_{SRH} closely approach or surpass the highest PCEs reported (see details and references in Table S2), demonstrating TMDs' strong potential for indoor applications. Although the ideal band gap for indoor PV is approximately 1.9 eV, closer to perovskites' band gap, TMDs with slightly lower band gaps can still achieve high PCEs under indoor lighting due to their ultrahigh absorption coefficients and favorable electronic properties. Perovskites at the moment achieve the highest PCE records for indoor PVs, but they suffer from stability issues, both in the dark and under illumination,[37] and use materials that raise environmental and health concerns.[18,38] In contrast, TMD solar cells avoid these drawbacks, being stable and free from toxic elements like lead, making them a safer and more sustainable choice for indoor applications. Moreover, advancements in TMD growth and device fabrication in the nanoelectronics industry[20,39–42] enable low-cost mass production of TMD solar cells,[43] rendering TMD solar cells an excellent candidate for indoor PVs.

Figure 7B compares the average power requirement of various IoT communications protocols and the range of power outputs from 10 cm^2 TMD solar cells under various indoor light spectra at 500 lux. It shows that the power output of these TMD solar cells is sufficient to support a range of low-power network protocols essential for IoT applications, such as RFID (Radio Frequency Identification), LoRA (Long Range) backscatter, passive Wi-Fi, BLE (Bluetooth Low Energy), ANT (Adaptive Network Topology), and Zigbee. These protocols are critical for ensuring efficient, reliable data transmission within indoor IoT networks. By meeting and potentially exceeding the power demands of current IoT protocols, TMD solar cells could be a key component in advancing sustainable IoT infrastructures.

Conclusions

We examined the potential of TMD solar cells for indoor energy harvesting, specifically assessing the performance of MoS_2,

$MoSe_2$, WS_2, and WSe_2 of various thicknesses and under various indoor lighting conditions, including CFL, LED, halogen, and low-light AM 1.5 G lighting. Our detailed balance model incorporates material-specific optical absorption data and accounts for various recombination mechanisms, including radiative, Auger, and SRH processes. We find that TMD solar cells can outperform existing indoor PV technologies, with PCE limits up to 36.5% under fluorescent, 35.6% under LED, 11.2% under halogen, and 27.6% under low-light AM 1.5 G lighting at 500 lux. With today's material quality, TMD solar cells can achieve up to 23.5% under fluorescent, 23.5% under LED, 5.9% under halogen, and 16.3% under low-light AM 1.5 G lighting at 500 lux. These efficiencies suggest the viability of TMD solar cells for powering IoT devices within indoor environments. Future work will need to focus on further refining the electrical and optical designs of TMD solar cells to fully capitalize on their high-efficiency potential and adapt them for broader commercial applications.

METHODS

The detailed balance equation governing the current density-voltage characteristics of the solar cell and the method to extract the performance metrics (i.e., J_{SC}, V_{OC}, FF, and PCE) is explained in detail in Note S1.

RESOURCE AVAILABILITY

Lead contact

Requests for further information and resources should be directed to and will be fulfilled by the lead contact, Eric Pop (epop@stanford.edu).

Materials availability

This study did not generate new materials.

Data and code availability

Code to replicate the main findings of this study can be found at https://doi.org/10.5281/zenodo.14760340.

ACKNOWLEDGMENTS

The authors acknowledge partial support from the Stanford Precourt Institute for Energy and the member companies of the SystemX Alliance at Stanford.

AUTHOR CONTRIBUTIONS

K.N.N. conceived the project. F.U.N. and K.N.N. developed the extended detailed balance model. F.U.N. implemented the model on TMDs, assisted by K.N.N. F.U.N., K.N.N., and E.P. contributed to data interpretation, presentation, and writing of the manuscript. E.P. supervised the work.

DECLARATION OF INTERESTS

The authors declare no competing interests.

SUPPLEMENTAL INFORMATION

Supplemental information can be found online at https://doi.org/10.1016/j.device.2025.100723.

Received: October 15, 2024
Revised: February 1, 2025
Accepted: February 5, 2025
Published: March 6, 2025

REFERENCES

1. Ramamurthy, S. (2016). Wireless Sensors: Technologies and Global Markets (BCC Research).
2. Mathews, I., Kantareddy, S.N., Buonassisi, T., and Peters, I.M. (2019). Technology and market perspective for indoor photovoltaic cells. Joule *3*, 1415–1426. https://doi.org/10.1016/j.joule.2019.03.026.
3. Yang, C.H., Hsueh, C.Y., Yeh, D.J., Ho, C.I., Leu, C.M., Yeh, Y.H., and Lee, S.C. (2011). Hydrogenated amorphous silicon solar cells on textured flexible substrate copied from a textured glass substrate template. IEEE Electron Device Lett. *32*, 1254–1256. https://doi.org/10.1109/LED.2011.2159259.
4. Chiba, Y., Islam, A., Watanabe, Y., Komiya, R., Koide, N., and Han, L. (2006). Dye-sensitized solar cells with conversion efficiency of 11.1%. Jpn. J. Appl. Phys. *47*, L638. https://doi.org/10.1143/JJAP.45.L638.
5. Michaels, H., Rinderle, M., Freitag, R., Benesperi, I., Edvinsson, T., Socher, R., Gagliardi, A., and Freitag, M. (2020). Dye-sensitized solar cells under ambient light powering machine learning: Towards autonomous smart sensors for the internet of things. Chem. Sci. *11*, 2895–2906. https://doi.org/10.1039/c9sc06145b.
6. Abdulrazzaq, O.A., Saini, V., Bourdo, S., Dervishi, E., and Biris, A.S. (2013). Organic solar cells: A review of materials, limitations, and possibilities for improvement. Part. Sci. Technol. *31*, 427–442. https://doi.org/10.1080/02726351.2013.769470.
7. Kang, H., Kim, G., Kim, J., Kwon, S., Kim, H., and Lee, K. (2016). Bulk-Heterojunction Organic Solar Cells: Five Core Technologies for Their Commercialization. Adv. Mater. *28*, 7821–7861. https://doi.org/10.1002/adma.201601197.
8. Li, Z., Zhang, J., Wu, S., Deng, X., Li, F., Liu, D., Lee, C., Lin, F., Lei, D., Chueh, C.-C., et al. (2020). Minimized surface deficiency on wide-bandgap perovskite for efficient indoor photovoltaics. Nano Energy *78*, 105377. https://doi.org/10.1016/j.nanoen.2020.105377.
9. Gong, O.Y., Han, G.S., Lee, S., Seo, M.K., Sohn, C., Yoon, G.W., Jang, J., Lee, J.M., Choi, J.H., Lee, D.-K., et al. (2022). Van der Waals force-assisted heat-transfer engineering for overcoming limited efficiency of flexible perovskite solar cells. ACS Energy Lett. *7*, 2893–2903. https://doi.org/10.1021/acsenergylett.2c01391.
10. Ann, M.H., Kim, J., Kim, M., Alosaimi, G., Kim, D., Ha, N.Y., Seidel, J., Park, N., Yun, J.S., and Kim, J.H. (2020). Device design rules and operation principles of high-power perovskite solar cells for indoor applications. Nano Energy *68*, 104321. https://doi.org/10.1016/j.nanoen.2019.104321.
11. Shimizu, T. (2004). Staebler-Wronski effect in hydrogenated amorphous silicon and related alloy films. Jpn. J. Appl. Phys. *43*, 3257. https://doi.org/10.1143/JJAP.43.3257.
12. Matsui, T., Bidiville, A., Maejima, K., Sai, H., Koida, T., Suezaki, T., Matsumoto, M., Saito, K., Yoshida, I., and Kondo, M. (2015). High-efficiency amorphous silicon solar cells: Impact of deposition rate on metastability. Appl. Phys. Lett. *106*, 053901. https://doi.org/10.1063/1.4907001.
13. Moser, M., Wadsworth, A., Gasparini, N., and McCulloch, I. (2021). Challenges to the Success of Commercial Organic Photovoltaic Products. Adv. Energy Mater. *11*, 2100056. https://doi.org/10.1002/aenm.202100056.
14. Xie, L., Song, W., Ge, J., Tang, B., Zhang, X., Wu, T., and Ge, Z. (2021). Recent progress of organic photovoltaics for indoor energy harvesting. Nano Energy *82*, 105770. https://doi.org/10.1016/j.nanoen.2021.105770.
15. Cui, Y., Hong, L., and Hou, J. (2020). Organic Photovoltaic Cells for Indoor Applications: Opportunities and Challenges. ACS Appl. Mater. Interfaces *12*, 38815–38828. https://doi.org/10.1021/acsami.0c10444.
16. Duan, L., Walter, D., Chang, N., Bullock, J., Kang, D., Phang, S.P., Weber, K., White, T., Macdonald, D., Catchpole, K., and Shen, H. (2023). Stability challenges for the commercialization of perovskite–silicon tandem solar cells. Nat. Rev. Mater. *8*, 261–281. https://doi.org/10.1038/s41578-022-00521-1.

17. Asghar, M.I., Zhang, J., Wang, H., and Lund, P.D. (2017). Device stability of perovskite solar cells – A review. Renew. Sustain. Energy Rev. *77*, 131–146. https://doi.org/10.1016/j.rser.2017.04.003.

18. Dixit, H., Boro, B., Ghosh, S., Paul, M., Kumar, A., and Singh, T. (2022). Assessment of lead-free tin halide perovskite solar cells using J–V hysteresis. Phys. Status Solidi *219*, 2100823. https://doi.org/10.1002/pssa.202100823.

19. Nassiri Nazif, K., Daus, A., Hong, J., Lee, N., Vaziri, S., Kumar, A., Nitta, F., Chen, M.E., Kananian, S., Islam, R., et al. (2021). High-specific-power flexible transition metal dichalcogenide solar cells. Nat. Commun. *12*, 7034. https://doi.org/10.1038/s41467-021-27195-7.

20. Nazif, K.N. (2021). Transition Metal Dichalcogenides for Next-Generation Photovoltaics (Stanford University).

21. Nassiri Nazif, K., Nitta, F.U., Daus, A., Saraswat, K.C., and Pop, E. (2023). Efficiency limit of transition metal dichalcogenide solar cells. Commun. Phys. *6*, 367. https://doi.org/10.1038/s42005-023-01447-y.

22. Tiedje, T., Yablonovitch, E., Cody, G.D., and Brooks, B.G. (1984). Limiting efficiency of silicon solar cells. IEEE Trans. Electron. Dev. *31*, 711–716. https://doi.org/10.1109/T-ED.1984.21594.

23. Freunek, M., Freunek, M., and Reindl, L.M. (2013). Maximum efficiencies of indoor photovoltaic devices. IEEE J. Photovoltaics *3*, 59–64. https://doi.org/10.1109/JPHOTOV.2012.2225023.

24. Handbook, I.E.S.L. (1966). IES Lighting Handbook (Illuminating Engineering Society).

25. Michael, P.R., Johnston, D.E., and Moreno, W. (2020). A conversion guide: solar irradiance and lux illuminance. J. meas. eng. *8*, 153–166. https://doi.org/10.21595/JME.2020.21667.

26. Went, C.M., Wong, J., Jahelka, P.R., Kelzenberg, M., Biswas, S., Hunt, M.S., Carbone, A., and Atwater, H.A. (2019). A new metal transfer process for van der Waals contacts to vertical Schottky-junction transition metal dichalcogenide photovoltaics. Sci. Adv. *5*, eaax6061. https://doi.org/10.1126/sciadv.aax6061.

27. Würfel, P., and Würfel, U. (2016). Physics of Solar Cells: From Basic Principles to Advanced Concepts (John Wiley & Sons).

28. Green, M.A. (1981). Solar cell fill factors: General graph and empirical expressions. Solid State Electron. *24*, 788–789. https://doi.org/10.1016/0038-1101(81)90062-9.

29. Yoshikawa, K., Kawasaki, H., Yoshida, W., Irie, T., Konishi, K., Nakano, K., Uto, T., Adachi, D., Kanematsu, M., Uzu, H., and Yamamoto, K. (2017). Silicon heterojunction solar cell with interdigitated back contacts for a photoconversion efficiency over 26%. Nat. Energy *2*, 17032. https://doi.org/10.1038/nenergy.2017.32.

30. Yu, Z., Raman, A., and Fan, S. (2010). Fundamental limit of nanophotonic light trapping in solar cells. Proc. Natl. Acad. Sci. USA *107*, 17491–17496. https://doi.org/10.1073/pnas.1008296107.

31. Svatek, S.A., Bueno-Blanco, C., Lin, D.-Y., Kerfoot, J., Macías, C., Zehender, M.H., Tobías, I., García-Linares, P., Taniguchi, T., Watanabe, K., et al. (2021). High open-circuit voltage in transition metal dichalcogenide solar cells. Nano Energy *79*, 105427. https://doi.org/10.1016/j.nanoen.2020.105427.

32. Nassiri Nazif, K., Kumar, A., Hong, J., Lee, N., Islam, R., McClellan, C.J., Karni, O., van de Groep, J., Heinz, T.F., Pop, E., et al. (2021). High-performance p–n junction transition metal dichalcogenide photovoltaic cells enabled by MoO x doping and passivation. Nano Lett. *21*, 3443–3450. https://doi.org/10.1021/acs.nanolett.1c00015.

33. Kim, K.-H., Andreev, M., Choi, S., Shim, J., Ahn, H., Lynch, J., Lee, T., Lee, J., Nazif, K.N., Kumar, A., et al. (2022). High-efficiency WSe_2 photovoltaic devices with electron-selective contacts. ACS Nano *16*, 8827–8836. https://doi.org/10.1021/acsnano.1c10054.

34. Wang, S., Yan, D., Ibarra Michel, J., Corletto, A., Wibowo, A.A., Balendhran, S., Lee, H.Y., Byun, S., Kim, S., Crozier, K.B., et al. (2024). Improved Efficiency in WSe2 Solar Cells Using Amorphous InO x Heterocontacts. ACS Nano *18*, 25046–25052. https://doi.org/10.1021/acsnano.4c06525.

35. Talla, V., Hessar, M., Kellogg, B., Najafi, A., Smith, J.R., and Gollakota, S. (2017). Lora backscatter: Enabling the vision of ubiquitous connectivity. Proc. ACM Interact. Mob. Wearable Ubiquitous Technol. *1*, 1–24. https://doi.org/10.1145/3130970.

36. Dementyev, A., Hodges, S., Taylor, S., and Smith, J. (2013). Power consumption analysis of Bluetooth Low Energy, ZigBee and ANT sensor nodes in a cyclic sleep scenario. In 2013 IEEE International Wireless Symposium (IWS), pp. 1–4. https://doi.org/10.1109/IEEE-IWS.2013.6616827.

37. Singh, R., Hu, H., Feeney, T., Diercks, A., Laufer, F., Li, Y., Duong, T., Schackmar, F., Nejand, B.A., and Paetzold, U.W. (2024). Danger in the Dark: Stability of Perovskite Solar Cells with Varied Stoichiometries and Morphologies Stressed at Various Conditions. ACS Appl. Mater. Interfaces *16*, 27450–27462. https://doi.org/10.1021/acsami.4c04350.

38. Fojtů, M., Teo, W.Z., and Pumera, M. (2017). Environmental impact and potential health risks of 2D nanomaterials. Environ. Sci. Nano *4*, 1617–1633. https://doi.org/10.1039/C7EN00401J.

39. Das, S., Sebastian, A., Pop, E., McClellan, C.J., Franklin, A.D., Grasser, T., Knobloch, T., Illarionov, Y., Penumatcha, A.V., Appenzeller, J., et al. (2021). Transistors based on two-dimensional materials for future integrated circuits. Nat. Electron. *4*, 786–799. https://doi.org/10.1038/s41928-021-00670-1.

40. Dorow, C.J., Penumatcha, A., Kitamura, A., Rogan, C., O'Brien, K.P., Lee, S., Ramamurthy, R., Cheng, C.-Y., Maxey, K., Zhong, T., et al. (2022). Gate length scaling beyond Si: mono-layer 2D channel FETs robust to short channel effects. In 2022 International Electron Devices Meeting (IEDM), pp. 5–7. https://doi.org/10.1109/IEDM45625.2022.10019524.

41. Chung, Y.-Y., Chou, B.-J., Hsu, C.-F., Yun, W.-S., Li, M.-Y., Su, S.-K., Liao, Y.-T., Lee, M.-C., Huang, G.-W., Liew, S.-L., et al. (2022). First Demonstration of GAA Monolayer-MoS_2 Nanosheet nFET with 410 μA/μm I_D 1 V V_D at 40 nm gate length. In 2022 International Electron Devices Meeting (IEDM), pp. 34–35. https://doi.org/10.1109/IEDM45625.2022.10019563.

42. Wu, X., Cott, D., Lin, Z., Shi, Y., Groven, B., Morin, P., Verreck, D., Smets, Q., Medina, H., Sutar, S., et al. (2021). Dual gate synthetic MoS_2 MOSFETs with 4.56 μF/cm^2 channel capacitance, 320 μS/μm G_m and 420 μA/μm I_d at 1V V_d/100nm L_g. In 2021 IEEE International Electron Devices Meeting (IEDM), pp. 4–7. https://doi.org/10.1109/IEDM19574.2021.9720695.

43. Neilson, K.M., Hamtaei, S., Nassiri Nazif, K., Carr, J.M., Rahimisheikh, S., Nitta, F.U., Brammertz, G., Blackburn, J.L., Hadermann, J., Saraswat, K.C., et al. (2024). Toward Mass Production of Transition Metal Dichalcogenide Solar Cells: Scalable Growth of Photovoltaic-Grade Multilayer WSe_2 by Tungsten Selenization. ACS Nano *18*, 24819–24828. https://doi.org/10.1021/acsnano.4c03590.

DEVICE, Volume *3*

Supplemental information

Transition metal dichalcogenide solar cells for indoor energy harvesting

Frederick U. Nitta, Koosha Nassiri Nazif, and Eric Pop

Table of Contents

Note S1. Extended detailed balance method incorporating radiative, Auger, SRH recombination, and free carrier absorption, and different indoor spectra

Based on the Tiedje-Yablonovitch model,[1] the detailed balance equation that defines the current density–voltage ($J-V$) characteristics of an optimized solar cell with an intrinsic or lightly-doped absorber film, characterized by equal electron (N) and hole density (P) under illumination, is applicable under the presence of radiative emission, Auger recombination, and free carrier absorption. The equation that governs this $J-V$ relationship is as follows:

$$\left(\alpha_1 + \frac{1}{4n^2L}\right)\exp\left(\frac{eV}{kT}\right)\int\int a_2(E)b_n(E,T)dE\,d\Omega + CN^3 = \frac{J_{\text{in}}}{eL}(1-f) \quad (1)$$

Here, α_1 is the free carrier absorption coefficient, n is the refractive index of the absorber film, L is the thickness of the film, e is the elementary charge, V is the output voltage, k is the Boltzmann constant, T is temperature, $a_2(E)$ is the absorptance (absorption probability) at photon energy E, $b_{\text{n}}(E,T)dEd\Omega$ is the flux of black-body photons for a photon energy interval dE and solid angle $d\Omega$ in a medium with refractive index of n, C is the Auger coefficient, N is the electron (and hole) density, $\frac{J_{\text{in}}}{eL}$ is the volume rate of generation of electron-hole pairs by the sun, and f is the fraction of the incident solar flux that is drawn off as current into the external circuit. $a_2(E)$, $b_{\text{n}}(E,T)$ and J_{in} are defined as:

$$a_2(E) = \frac{\alpha_2(E)}{\alpha_2(E) + \alpha_1(E) + \frac{1}{4n^2L}} \quad (2)$$

$$b_{\text{n}}(E,T) = \frac{2}{h^3}\frac{n^2}{c^2}E^2\exp\left(\frac{1}{\frac{E}{kT}-1}\right) \quad (3)$$

$$J_{\text{in}} = \int eS(E)a_2(E)dE \quad (4)$$

where $\alpha_2(E)$ is the optical absorption coefficient at photon energy E, h is the Planck constant, c is the speed of light in vacuum, and $S(E)$ is the one of the four indoor spectra we employed for this work. In **Equation (1)**, the terms on the left-hand side sequentially represent the rates of free carrier absorption, radiative emission, and Auger recombination. Conversely, the terms on the right-hand side describe the generation rate of electron-hole pairs and the solar cell's output current, respectively. To include Shockley-Read-Hall (SRH) recombination into this model, we add SRH recombination rate U_{SRH} to the left-hand side of **Equation (1)**:

$$\left(\alpha_1 + \frac{1}{4n^2L}\right)\exp\left(\frac{eV}{kT}\right)\int\int a_2(E)b_n(E,T)dE\,d\Omega + CN^3 + U_{\text{SRH}} = \frac{J_{\text{in}}}{eL}(1-f) \quad (5)$$

Carrier lifetimes associated with each recombination mechanism, τ_{e} and τ_{h} for electrons and holes, respectively, can be defined as:

$$\tau_{\text{e}} = \frac{\Delta N}{U} \quad (6)$$

$$\tau_h = \frac{\Delta P}{U} \quad (7)$$

where ΔN and ΔP are the disturbances of the electron and hole populations from their equilibrium values N_0 and P_0, respectively, and U is the recombination rate. For an intrinsic or lightly-doped absorber film under illumination:

$$N = P \gg N_0, P_0 \quad (8)$$

$$\Delta N = \Delta P \approx N \quad (9)$$

Thus, the SRH recombination rate can be written as:

$$U_{\mathrm{SRH}} = \frac{N}{\tau_{\mathrm{SRH}}} \tag{10}$$

Combining **Equations (5)** and **(10)** leads to the following:

$$\left(\alpha_1 + \frac{1}{4n^2L}\right)\exp\left(\frac{eV}{kT}\right)\int\int a_2(E)b_n(E,T)dE\,d\Omega + CN^3 + \frac{N}{\tau_{\mathrm{SRH}}} = \frac{J_{\mathrm{in}}}{eL}(1-f) \tag{11}$$

Equation (11) represents the detailed balance equation governing the current density–voltage characteristics of optimized solar cell having an intrinsic or lightly-doped absorber film (i.e., *N* = *P* under illumination) in the presence of radiative emission, Auger recombination, free carrier absorption, and SRH recombination with the characteristic carrier lifetime τ_{SRH}. In the absence of free carrier absorption, **Equation (11)** simplifies further:

$$J_0\exp\left(\frac{eV}{kT}\right) + eLCN_i^3 exp\left(\frac{3eV}{2kT}\right) + \frac{eL}{\tau_{\mathrm{SRH}}}N_i\exp\left(\frac{eV}{2kT}\right) = J_{\mathrm{in}}(1-f) \tag{12}$$

where N_i is the intrinsic carrier density and J_0 is defined as:

$$J_0 = e\pi\int b_1(E)a_2(E)dE \tag{13}$$

To derive the current density–voltage characteristics of the solar cell, f is varied from zero to one, which corresponds to output current density (J) of zero to J_{in}. The output voltage (V) is then calculated by solving **Equation (12).** From these $J-V$ characteristics, performance metrics are extracted as follows:

$$V_{\mathrm{OC}} = V(J=0) \tag{14}$$

$$J_{\mathrm{SC}} = J(V=0) \tag{15}$$

$$P_{\mathrm{MPP}} = \max(I\cdot V) = I\cdot V\left(\frac{d(I\cdot V)}{dV} = 0\right) \tag{16}$$

$$FF = \frac{P_{\mathrm{MPP}}}{V_{\mathrm{OC}}\cdot J_{\mathrm{SC}}} \tag{17}$$

$$PCE = \frac{P_{MPP}}{P_{in}} \tag{18}$$

where V_{OC} is the open-circuit voltage, J_{SC} is the short-circuit current density, P_{MPP} is power density at maximum power point (MPP), FF is the fill factor, and PCE is power conversion efficiency of the solar cell. P_{in}, the input power density, depends on the spectra and the lux level, and the calculated values are listed in **Table S1**.

Note S2. Extrapolation of Halogen Lamp Spectrum Using Blackbody Radiation Formula

Halogen lamps, which operate by heating a tungsten filament to high temperatures within a halogen gas, closely mimic the emission characteristics of a blackbody radiator.[2] This similarity allows for the use of the blackbody radiation formula to extend the lamp's spectral data,[3] which did not cover the full range of photon energies emitted, especially at lower energy (higher wavelengths). We employed Planck's law of blackbody radiation,[4] expressed as

$$B_\nu(\nu, T) = \frac{2h\nu^3}{c^2}\frac{1}{e^{\frac{h\nu}{kT}}-1} \tag{19}$$

where h is Planck's constant, ν is the frequency of radiation, c is the speed of light in vacuum, k is Boltzmann's constant. The absolute temperature T of the blackbody is 2847 K, which was determined from the fitting of experimental data to **Equation (19)**. This fit is shown in **Figure S1**.

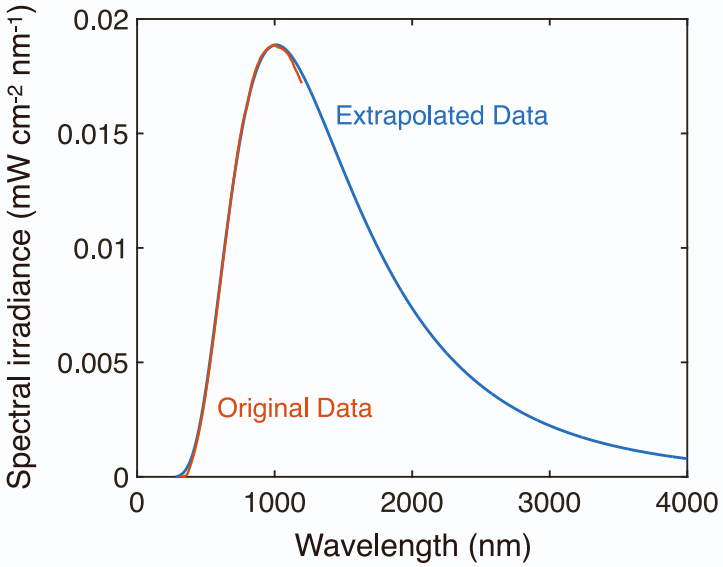

Figure S1. Extrapolation of halogen spectrum at 500 lux. The original (experimental) data is in orange, our extrapolation in blue. The extrapolation was performed using the blackbody radiation formula detailed in **Note S2**. The precision of this method was confirmed by an R-square value of 1.00 and root mean square error (RMSE) of 2.64×10^{-5}.

Table S1. Input power density across different lighting conditions. The input power densities (mW cm^{-2}) for different light sources across varying illumination levels.

	Parking garage (50 lux)	Warehouse (150 lux)	Office (400 lux)	Retail store (500 lux)
Compact fluorescent lamp (CFL)	0.145	0.434	1.157	1.447
Light-emitting diode (LED)	0.175	0.526	1.402	1.752
Halogen	2.605	7.814	20.837	26.047
AM 1.5 G	0.432	1.297	3.459	4.324

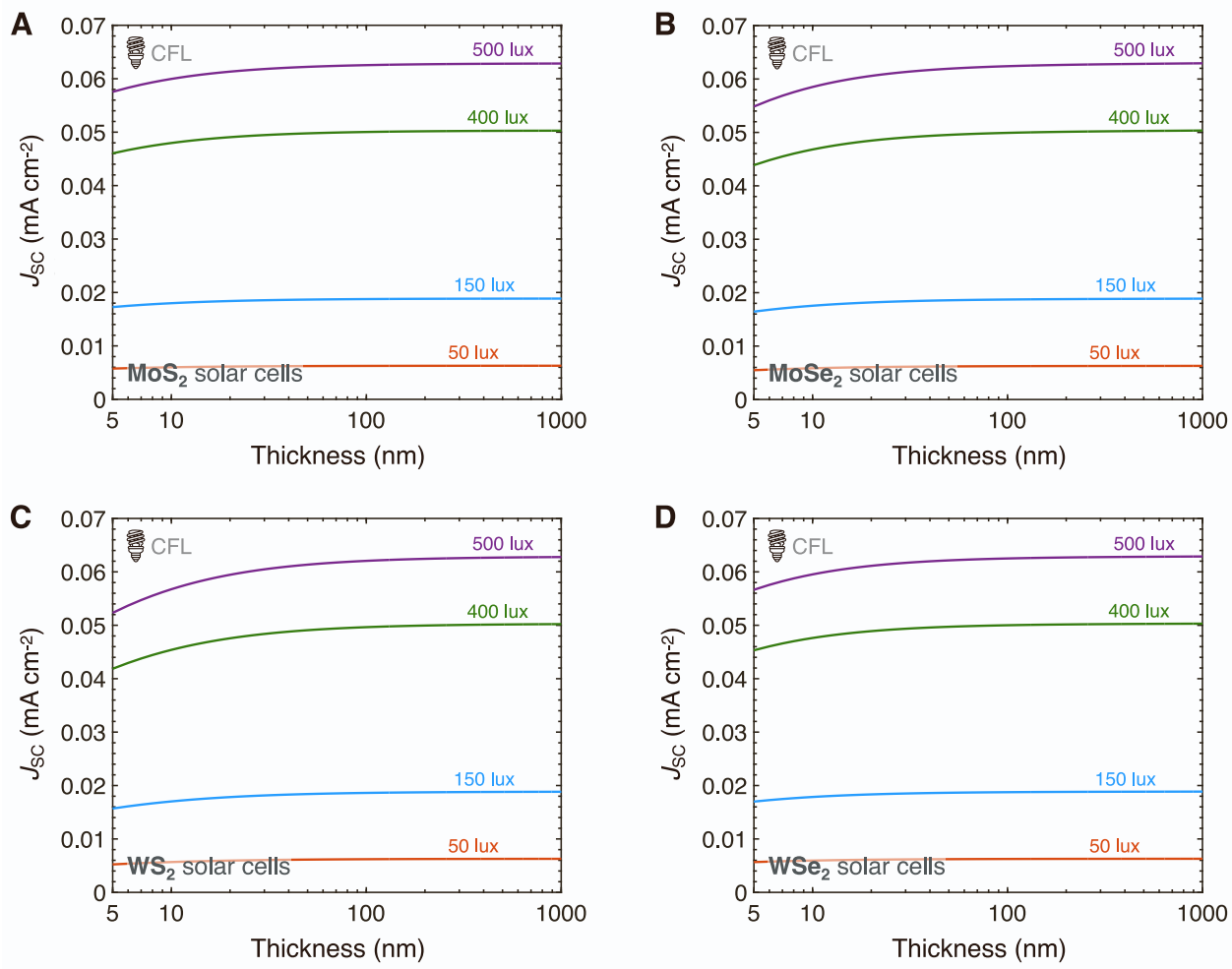

Figure S2. Short-circuit current density (J_{SC}) of thin-film TMD solar cells under compact fluorescent lamp (CFL) illumination. J_{SC} of (A) MoS_2, (B) $MoSe_2$, (C) WS_2, and (D) WSe_2 solar cells as a function of the TMD (absorber) film thickness and CFL illumination intensity at 300 K. Four CFL illumination intensities correspond to the four colors, as labeled (e.g. purple is at 500 lux). The J_{SC} exhibits minimal improvement with increased film thickness at lower light intensities such as parking garages (50 lux) or warehouses (150 lux), reflecting near-unity absorption for higher-energy photons (above ~2.0 eV),[5–7] which dominate the CFL spectrum at these intensities. In contrast, at higher intensities found in office (400 lux) or retail store (500 lux) settings, J_{SC} shows more improvement as the film thickness increases, attributable to enhanced absorption of lower-energy photons (below ~2.0 eV). At higher film thicknesses, the J_{SC} values for all materials start to plateau as the absorption reaches near-complete across the CFL spectrum's most relevant energy range, from ~1.5 eV to ~3.5 eV. This indicates that the materials have achieved their maximum potential for light absorption in this spectrum, and making the films thicker beyond this point will not increase the photocurrent.

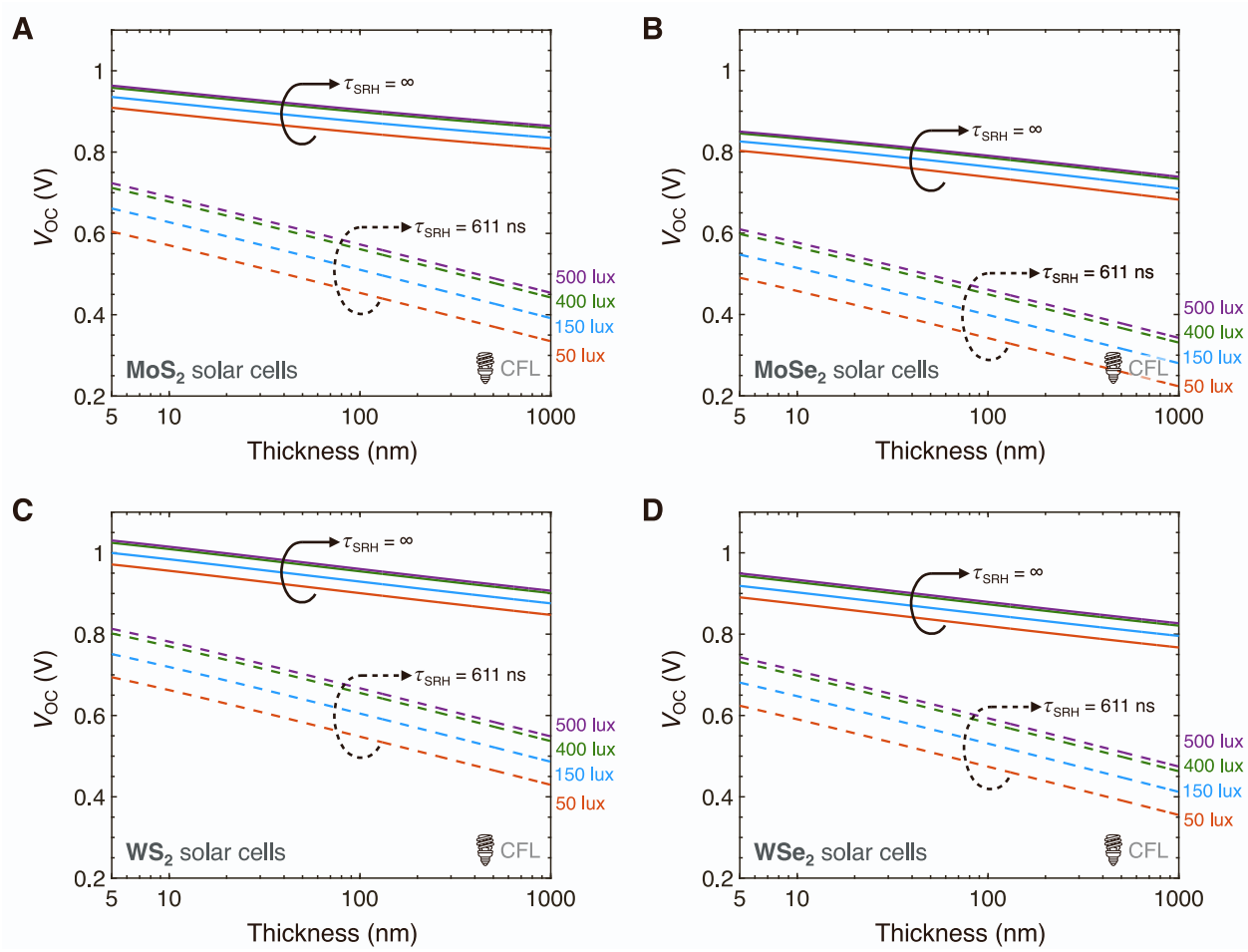

Figure S3. Open-circuit voltage (V_{OC}) of thin-film TMD solar cells under CFL illumination. V_{OC} of (A) MoS_2, (B) $MoSe_2$, (C) WS_2, and (D) WSe_2 solar cells as a function of TMD film thickness, material quality (τ_{SRH}), and CFL illumination intensity at 300 K. τ_{SRH}, Shockley-Read-Hall (SRH) lifetime. Solid lines are in the limit defect-free material (no SRH recombination), dashed lines with τ_{SRH} = 611 ns. Four CFL illumination intensities correspond to the four colors, as labeled (e.g. purple dashed and solid are at 500 lux). V_{OC} exhibits a logarithmic decline with decreasing light intensity, reflecting its direct proportionality to the logarithm of the photocurrent, which is dependent on light intensity. Additionally, V_{OC} decreases with increasing film thickness, more notably for films with an SRH lifetime of 611 ns. This decrease can be partially attributed to a shift in the absorption threshold towards lower photon energies as films become thicker,[5] effectively reducing the band gap and thus V_{OC}. The increase in film thickness also leads to higher light absorption and charge carrier densities, escalating the likelihood of both radiative and non-radiative recombination events. The pronounced V_{OC} decline with τ_{SRH} = 611 ns underscores the impact of material quality on maintaining high V_{OC} across various lighting conditions.

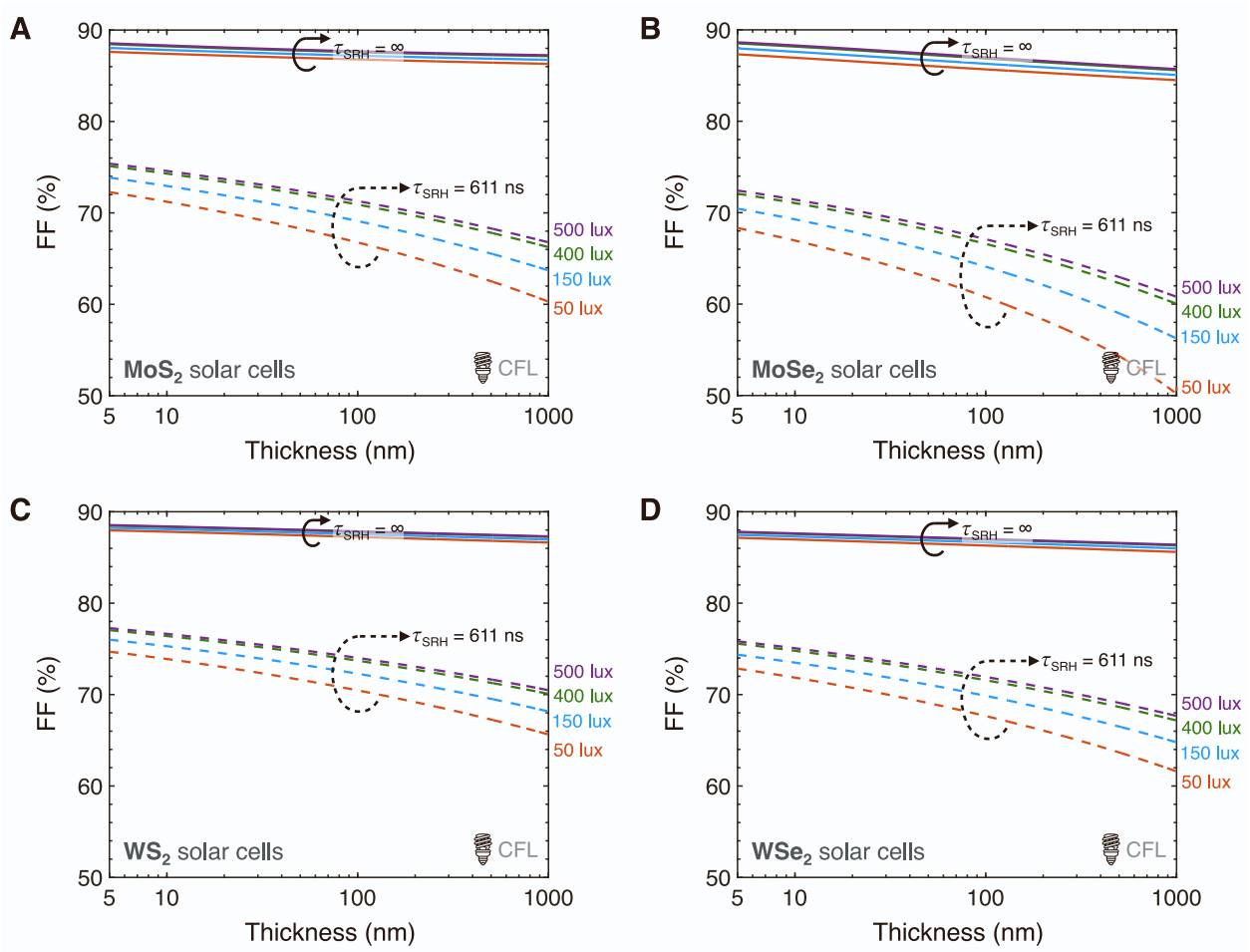

Figure S4. Fill factor (FF) of thin-film TMD solar cells under CFL illumination. FF of (A) MoS_2, (B) $MoSe_2$, (C) WS_2, and (D) WSe_2 solar cells as a function of TMD film thickness, material quality (τ_{SRH}), and CFL illumination intensity at 300 K. τ_{SRH}, Shockley-Read-Hall (SRH) lifetime. Solid lines are in the limit defect-free material (no SRH recombination), dashed lines with τ_{SRH} = 611 ns. Four CFL illumination intensities correspond to the four colors, as labeled (e.g. purple dashed and solid are at 500 lux). It is established that a higher V_{OC} generally leads to a higher FF due to reduced recombination losses.[8] When considering a τ_{SRH} of 611 ns, the drop in both V_{OC} and FF with increased film thickness is more pronounced, particularly under lower light intensities. This is because lower light intensities reduce carrier generation, and although SRH recombination itself decreases with lower carrier densities, the relative impact of each recombination event is greater when fewer carriers are available. As a result, both V_{OC} and FF decline more sharply in these conditions, especially in thicker films where defects are more prominent. The more pronounced the SRH recombination, the greater the impact on the ideality factor of the diode and consequently on FF. This lines up with the understanding that the closer the ideality factor is to unity (as in the case of infinite τ_{SRH}), the higher the FF, whereas dominant SRH recombination leads to an ideality factor of 2, reducing the FF. The dependence of FF on V_{OC} also explains why FF decreases with increasing film thickness. As shown in **Figure S3**, V_{OC} decreases with increasing film thickness, and FF here follows the same trend.

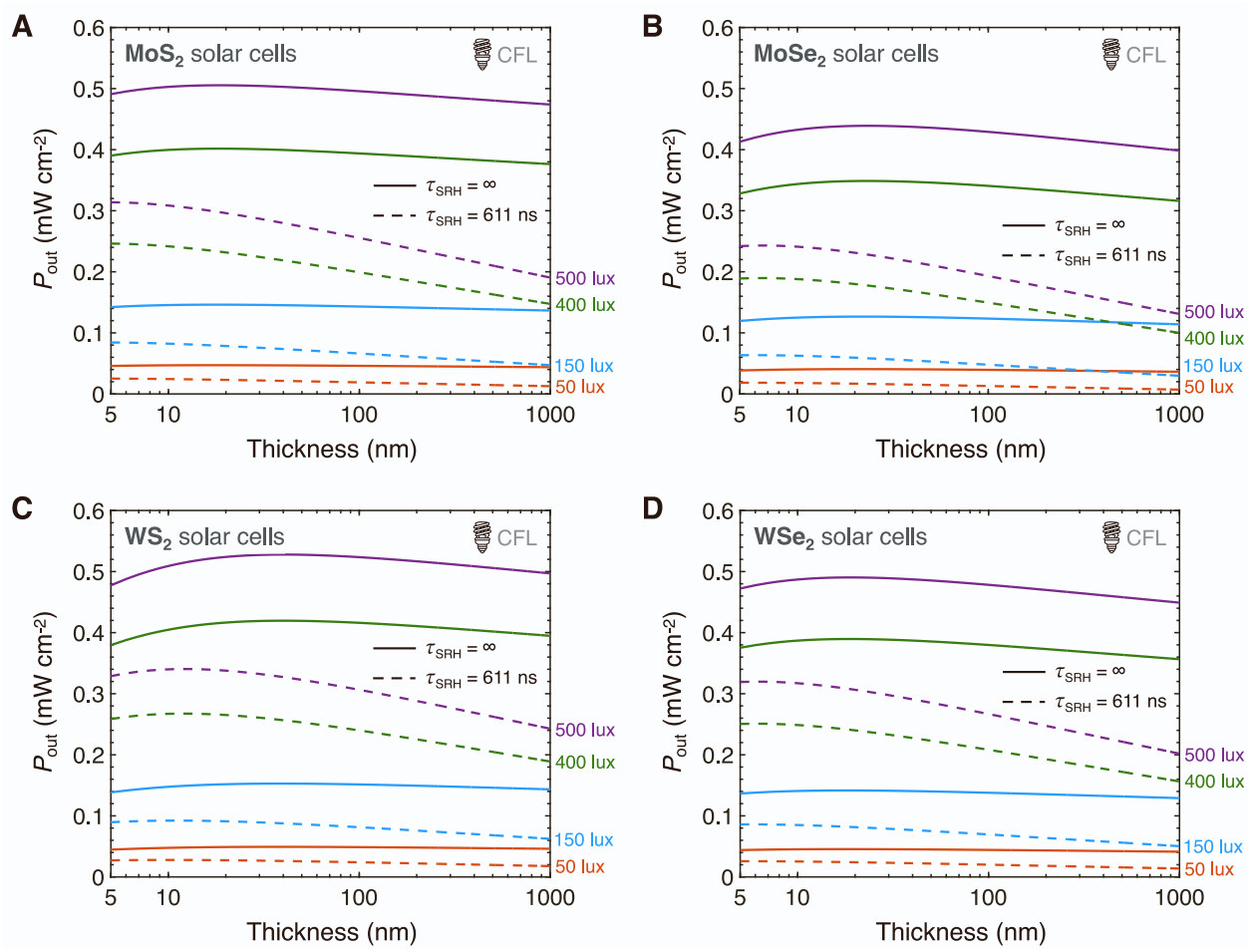

Figure S5. Output power (P_{out}) of thin-film TMD solar cells under CFL illumination. P_{out} of (A) MoS_2, (B) $MoSe_2$, (C) WS_2, and (D) WSe_2 solar cells as a function of TMD film thickness, material quality (τ_{SRH}), and CFL illumination intensity at 300 K. τ_{SRH}, Shockley-Read-Hall (SRH) lifetime. Solid lines are in the limit defect-free material (no SRH recombination), dashed lines with τ_{SRH} = 611 ns. Four CFL illumination intensities correspond to the four colors, as labeled (e.g. purple dashed and solid are at 500 lux). Since P_{out} of solar cells is the product of J_{SC}, V_{OC}, and FF, these trends are explained by the J_{SC}, V_{OC}, and fill factor trends in **Figure S2, Figure S3**, and **Figure S4**, respectively. As observed, the output power curves exhibit an inverted U-shape, which can be explained by the competing in-fluences of J_{SC} (**Figure S2**) and the product of V_{OC} (**Figure S3**) and FF (**Figure S4**). As the film thickness increases, J_{SC} improves due to enhanced light absorption; however, this benefit is counterbalanced by the degradation of V_{OC} and FF, which is particularly pronounced when τ_{SRH} is finite at 611 ns. At lower light intensities (e.g., 50 lux), J_{SC} does not increase substantially with increasing thickness (**Figure S2**). Similarly, for the infinite τ_{SRH} scenario (no SRH recombination), V_{OC} and FF experience a mild drop with thickness (**Figure S3** and **Figure S4**). Therefore, the improvement in J_{SC} with thickness is offset by losses in V_{OC} and FF, resulting in a constant P_{out} across the range of film thicknesses considered. SRH recombination, however, leads to steeper decline in V_{OC} and fill factor with thickness (**Figure S3** and **Figure S4**), leading to decreasing P_{out} with increasing thickness. This behavior underscores the critical role that material quality and defect minimization plays in optimizing the power output of TMD-based solar cells.

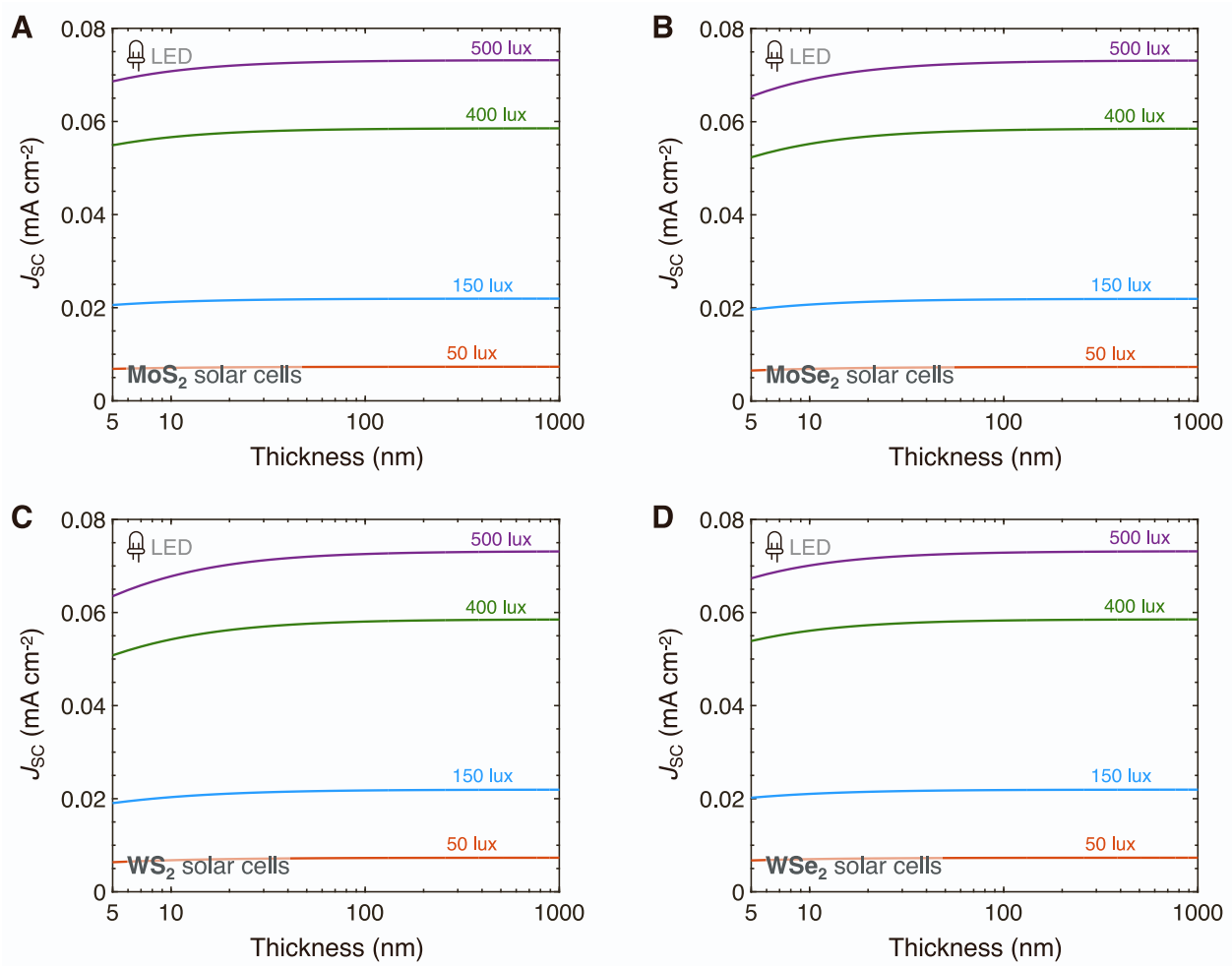

Figure S6. Short-circuit current density (J_{SC}) of thin-film TMD solar cells under LED illumination. J_{SC} of (A) MoS_2, (B) $MoSe_2$, (C) WS_2, and (D) WSe_2 solar cells as a function of the TMD (absorber) film thickness and LED illumination intensity at 300 K. Four LED illumination intensities correspond to the four colors, as labeled (e.g. purple is at 500 lux). Similar to CFL lighting, under LED illumination, J_{SC} enhancement with film thickness is modest at low intensities, like in parking garages (50 lux) and warehouses (150 lux), but better at higher intensities found in offices (400 lux) and retail stores (500 lux). The slightly higher J_{SC} values under LED compared to CFL lighting can be attributed to the LED spectrum aligning less with the CIE Photopic Luminosity Function than CFL. Consequently, LED sources require more emitted light to achieve the same lux levels (**Table S1**), which increases the available photon flux for energy conversion. For all TMD materials, J_{SC} varies more distinctly at lower thicknesses under LED light. The LED spectrum's broader photon energy range at higher intensities allows for increased J_{SC} in thicker films due to absorption of lower-energy photons. At higher thicknesses, J_{SC} plateaus for all materials, indicating maximum potential absorption in the relevant energy range of LED light.

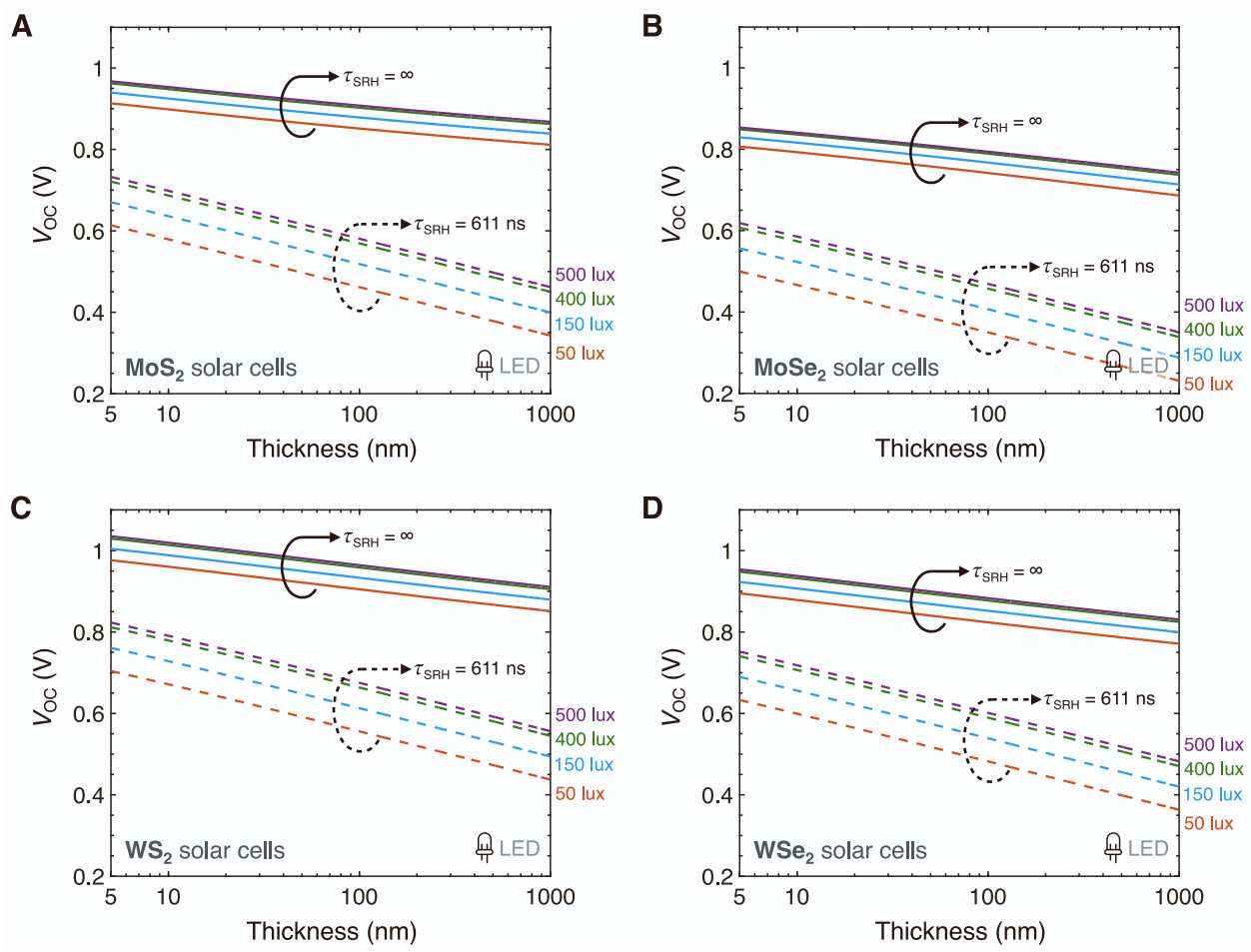

Figure S7. Open-circuit voltage (V_{OC}) of thin-film TMD solar cells under LED illumination. V_{OC} of (A) MoS_2, (B) $MoSe_2$, (C) WS_2, and (D) WSe_2 solar cells as a function of TMD film thickness, material quality (τ_{SRH}), and LED illumination intensity at 300 K. τ_{SRH}, Shockley-Read-Hall (SRH) lifetime. Solid lines are in the limit defect-free material (no SRH recombination), dashed lines with τ_{SRH} = 611 ns. Four LED illumination intensities correspond to the four colors, as labeled (e.g. purple dashed and solid are at 500 lux). With increasing TMD film thickness, there is a noticeable reduction in V_{OC}, particularly when considering a finite SRH lifetime. This reduction is consistent with what was observed under CFL lighting. As film thickness grows, the absorption threshold shifts, diminishing the effective band gap and thus the V_{OC}[5]. The resulting higher carrier densities from this shift elevate recombination rates, with non-radiative processes having a more significant impact under finite SRH conditions. This relationship showcases the critical effect of material defects on V_{OC}, underlining the importance of advancing material quality for improved TMD solar cell performance.

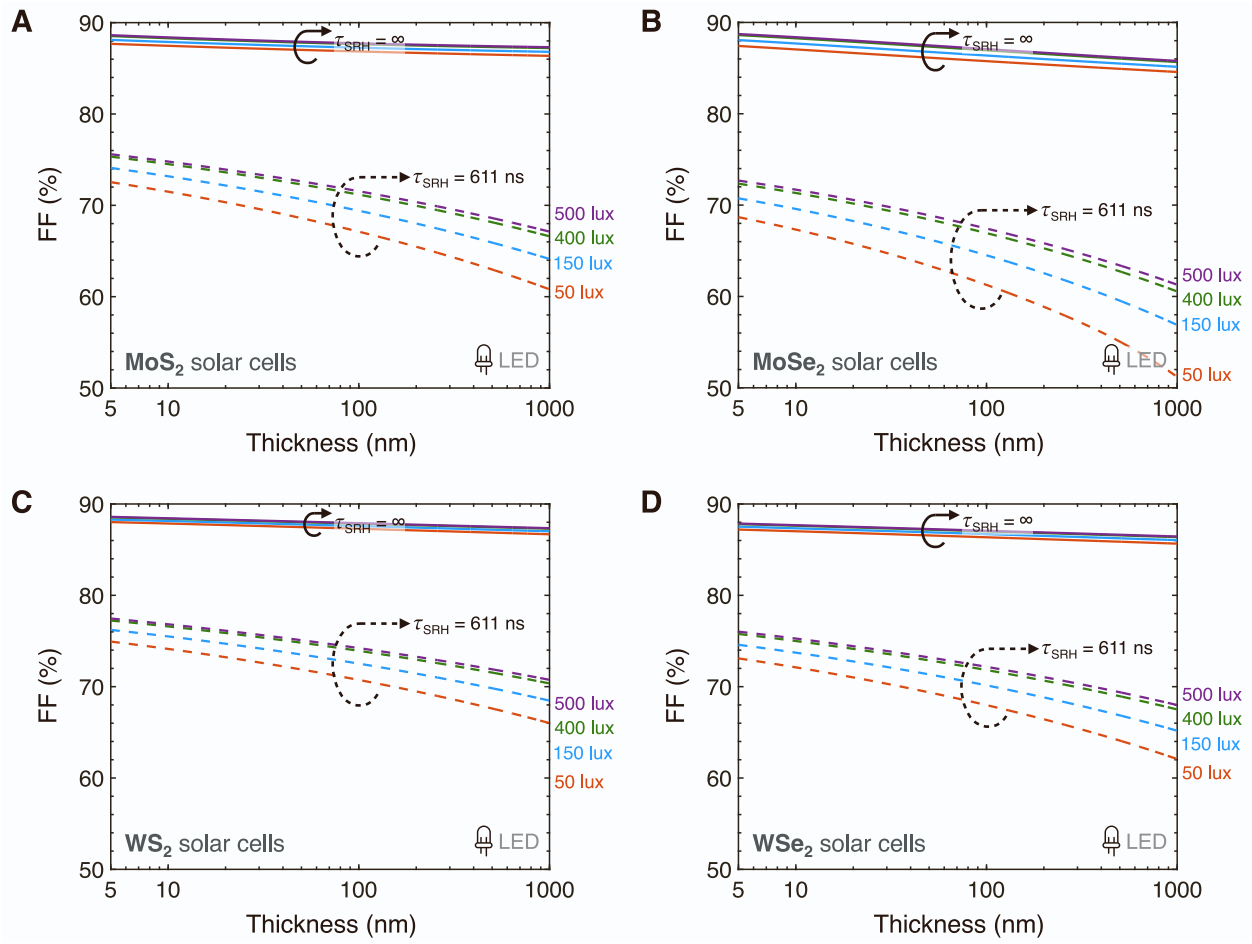

Figure S8. Fill factor (FF) of thin-film TMD solar cells under LED illumination. FF of (A) MoS_2, (B) $MoSe_2$, (C) WS_2, and (D) WSe_2 solar cells as a function of TMD film thickness, material quality (τ_{SRH}), and LED illumination intensity at 300 K. τ_{SRH}, Shockley-Read-Hall (SRH) lifetime. Solid lines are in the limit defect-free material (no SRH recombination), dashed lines with τ_{SRH} = 611 ns. Four LED illumination intensities correspond to the four colors, as labeled (e.g. purple dashed and solid are at 500 lux). As illumination intensity increases, V_{OC} and consequently FF generally improve due to increased carrier generation, which helps reduce the relative impact of recombination losses. Under infinite τ_{SRH} conditions, FF is almost independent of light intensity and film thickness, indicating a dominant role for non-radiative recombination. The consistency of FF values across all thicknesses in the infinite τ_{SRH} case contrasts with the decline observed at finite τ_{SRH}. When τ_{SRH} is finite (e.g., 611 ns), FF shows a more pronounced decrease with increasing film thickness, particularly at lower light intensities. This is because thicker films absorb more light, generating more carriers, but also increasing the likelihood of carrier recombination at defect sites, especially when material quality is lower (as indicated by a finite τ_{SRH}). At lower light intensities, while fewer carriers are generated overall, the relative impact of defects is greater because fewer carriers are available to be collected.

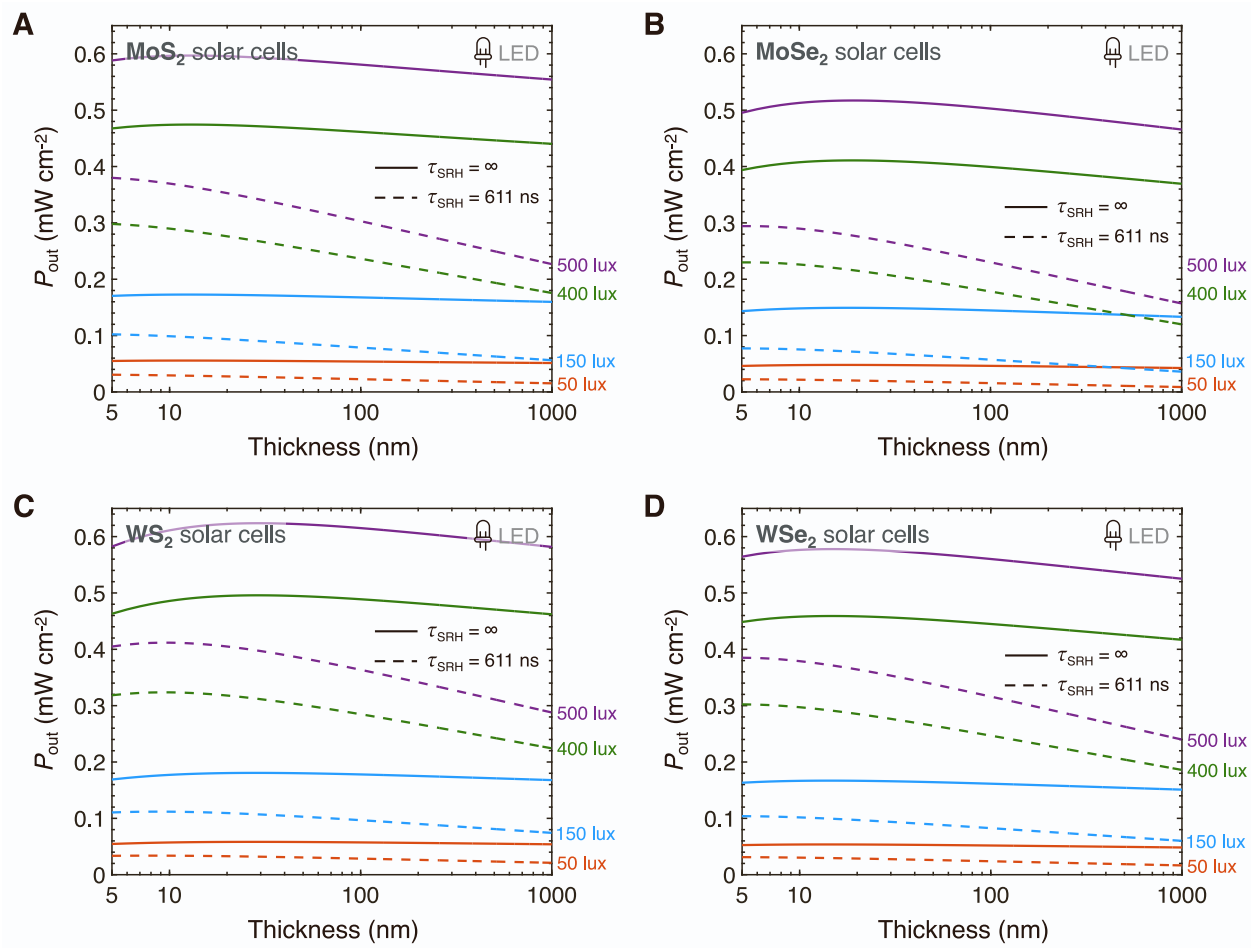

Figure S9. Output power (P_{out}) of thin-film TMD solar cells under LED illumination. P_{out} of (A) MoS_2, (B) $MoSe_2$, (C) WS_2, and (D) WSe_2 solar cells as a function of TMD film thickness, material quality (τ_{SRH}), and LED illumination intensity at 300 K. τ_{SRH}, Shockley-Read-Hall (SRH) lifetime. Solid lines are in the limit defect-free material (no SRH recombination), dashed lines with τ_{SRH} = 611 ns. Four LED illumination intensities correspond to the four colors, as labeled (e.g. purple dashed and solid are at 500 lux). Under LED lighting, similar to CFL illumination, P_{out} demonstrates a dependence on J_{SC}, V_{OC}, and FF behaviors in **Figure S6**, **Figure S7**, and **Figure S8**, respectively. At lower light intensities (e.g., 50 lux), the P_{out}'s peak is less distinct due to the modest increase in J_{SC} with film thickness. P_{out} is influenced by the trade-off between enhanced J_{SC} from increased thickness and the reductions in V_{OC} and FF, which is especially noticeable at finite τ_{SRH}. For infinite τ_{SRH}, P_{out} changes less across film thicknesses since V_{OC} and FF are more constant. This results in a flatter P_{out} curve, indicating that defects and SRH recombination have a larger effect on P_{out} than radiative and Auger recombination. The variation in P_{out} between the different material qualities (τ_{SRH} values) underlines the importance of material quality and defect control.

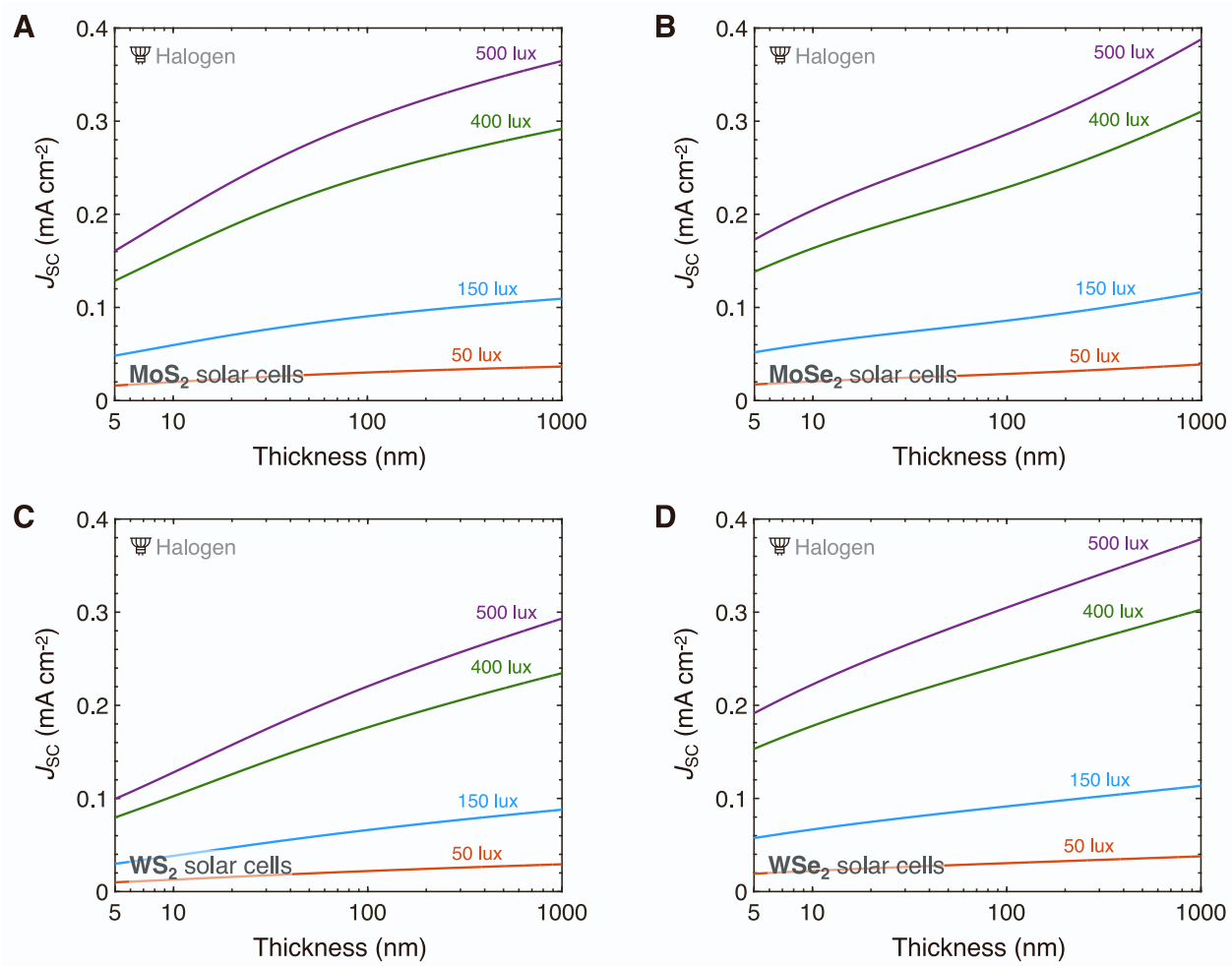

Figure S10. Short-circuit current density (J_{SC}) of thin-film TMD solar cells under halogen illumination. J_{SC} of (A) MoS_2, (B) $MoSe_2$, (C) WS_2, and (D) WSe_2 solar cells as a function of the TMD (absorber) film thickness and halogen illumination intensity at 300 K. Four halogen illumination intensities correspond to the four colors, as labeled (e.g. purple is at 500 lux). Like with CFL lighting, there is less J_{SC} improvement at lower light intensities under halogen lighting, yet the increase is more compared to CFL due to the halogen bulb's broader spectral coverage. Under halogen lighting, J_{SC} is comparatively higher than under CFL due to the spectral characteristics of halogen light. Halogen bulbs emit across a broader spectral range with less overlap with the CIE Photopic Luminosity Function than CFL sources, requiring more intensity to achieve the same perceived brightness (**Table S1**). This wider distribution of energy across the spectrum leads to enhanced J_{SC} values for TMD solar cells.

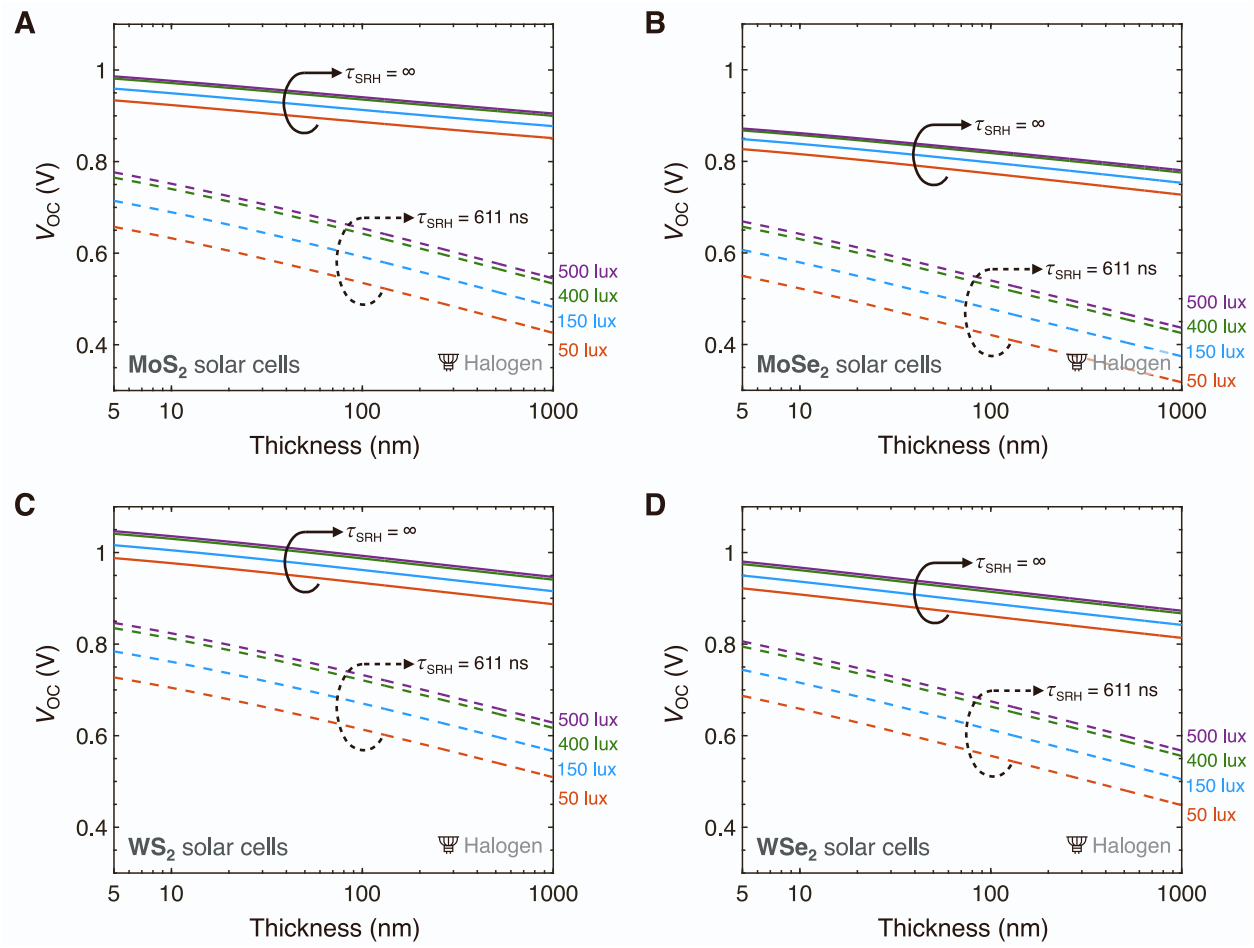

Figure S11. Open-circuit voltage (V_{OC}) of thin-film TMD solar cells under halogen illumination. V_{OC} of (A) MoS_2, (B) $MoSe_2$, (C) WS_2, and (D) WSe_2 solar cells as a function of TMD film thickness, material quality (τ_{SRH}), and halogen illumination intensity at 300 K. τ_{SRH}, Shockley-Read-Hall (SRH) lifetime. Solid lines are in the limit defect-free material (no SRH recombination), dashed lines with τ_{SRH} = 611 ns. Four halogen illumination intensities correspond to the four colors, as labeled (e.g. purple dashed and solid are at 500 lux). Similar to CFL and LED lighting, V_{OC} decreases with an increase in film thickness, more noticeably at the finite SRH lifetime of 611 ns due to increased recombination at defect sites. This reduction is attributed to the shift in absorption threshold with thicker films, resulting in a lower effective band gap and higher carrier densities that enhance recombination.[5]

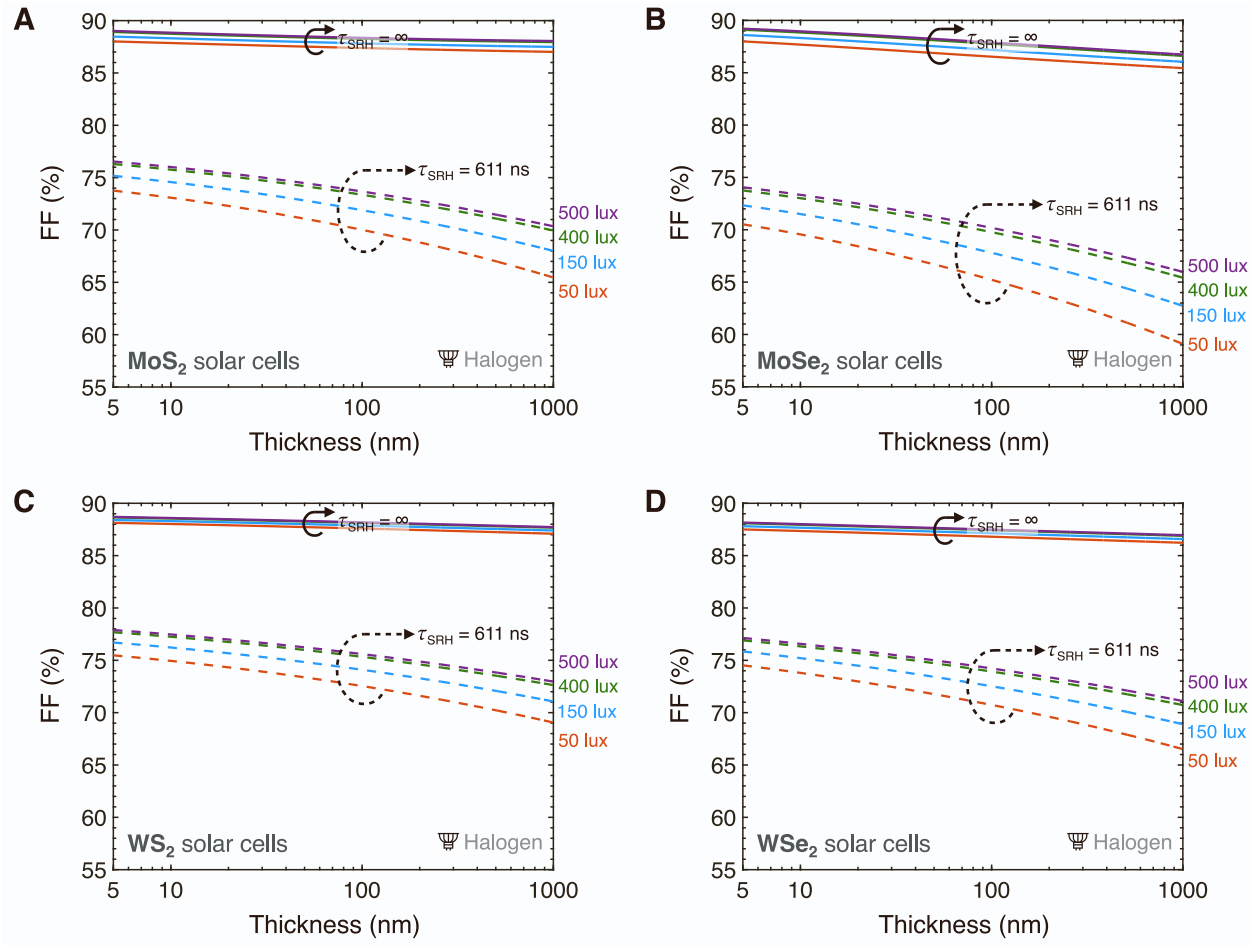

Figure S12. Fill factor (FF) of thin-film TMD solar cells under halogen illumination. FF of (A) MoS_2, (B) $MoSe_2$, (C) WS_2, and (D) WSe_2 cells as a function of TMD film thickness, material quality (τ_{SRH}), and halogen illumination intensity at 300 K. τ_{SRH}, Shockley-Read-Hall (SRH) lifetime. Solid lines are in the limit defect-free material (no SRH recombination), dashed lines with τ_{SRH} = 611 ns. Four halogen illumination intensities correspond to the four colors, as labeled (e.g. purple dashed and solid are at 500 lux). With a τ_{SRH} of 611 ns, the decrease in V_{OC} and consequently FF becomes more pronounced as film thickness increases, particularly under lower light intensities. This is because, at lower light intensities, fewer carriers are generated, and any losses due to recombination at defect sites have a disproportionately larger impact on the FF. In thicker films, where there are more potential defect sites, this effect is even more pronounced. Across the TMD materials, FF is quite uniform at all thicknesses for an infinite τ_{SRH}, suggesting minimal radiative and Auger recombination. In contrast, for a finite τ_{SRH}, FF begin the same at lower thicknesses but spread out as the films get thicker. This spread results from how each material's carrier density affects non-radiative recombination, which alters the FF.

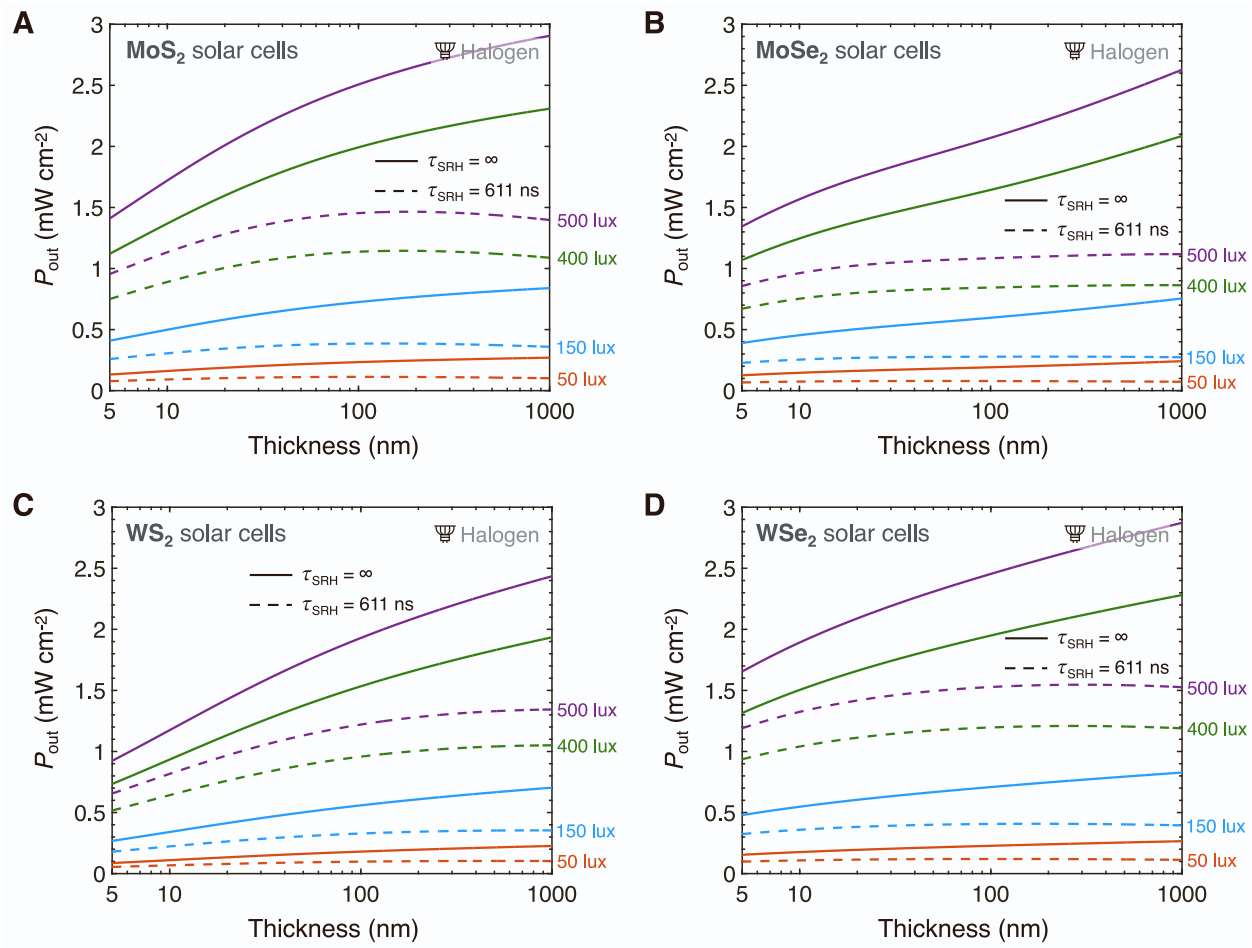

Figure S13. Output power (P_{out}) of thin-film TMD solar cells under halogen illumination. P_{out} of (A) MoS_2, (B) $MoSe_2$, (C) WS_2, and (D) WSe_2 solar cells as a function of TMD film thickness, material quality (τ_{SRH}), and halogen illumination intensity at 300 K. τ_{SRH}, Shockley-Read-Hall (SRH) lifetime. Solid lines are in the limit defect-free material (no SRH recombination), dashed lines with τ_{SRH} = 611 ns. Four halogen illumination intensities correspond to the four colors, as labeled (e.g. purple dashed and solid are at 500 lux). For an infinite SRH lifetime, P_{out} for all materials consistently rises without a peak, implying that the positive effects of increased J_{SC} with thickness (**Figure S10**) outweigh the negative impacts on V_{OC} (**Figure S11**) and FF (**Figure S12**). This trend suggests that halogen light, with its broad spectrum, may be effectively utilized by thicker TMD films without the penalties of increased recombination from defects. In contrast, for a finite τ_{SRH} of 611 ns, MoS_2 and WSe_2 display peaks in P_{out} at certain thicknesses. This indicates that there are optimal thicknesses at which the benefits of increased absorption (and hence J_{SC}) surpass the detriments caused by higher recombination rates affecting V_{OC} and FF, and beyond a certain film thickness, the additional material thickness does not proportionally contribute to power generation under halogen illumination.

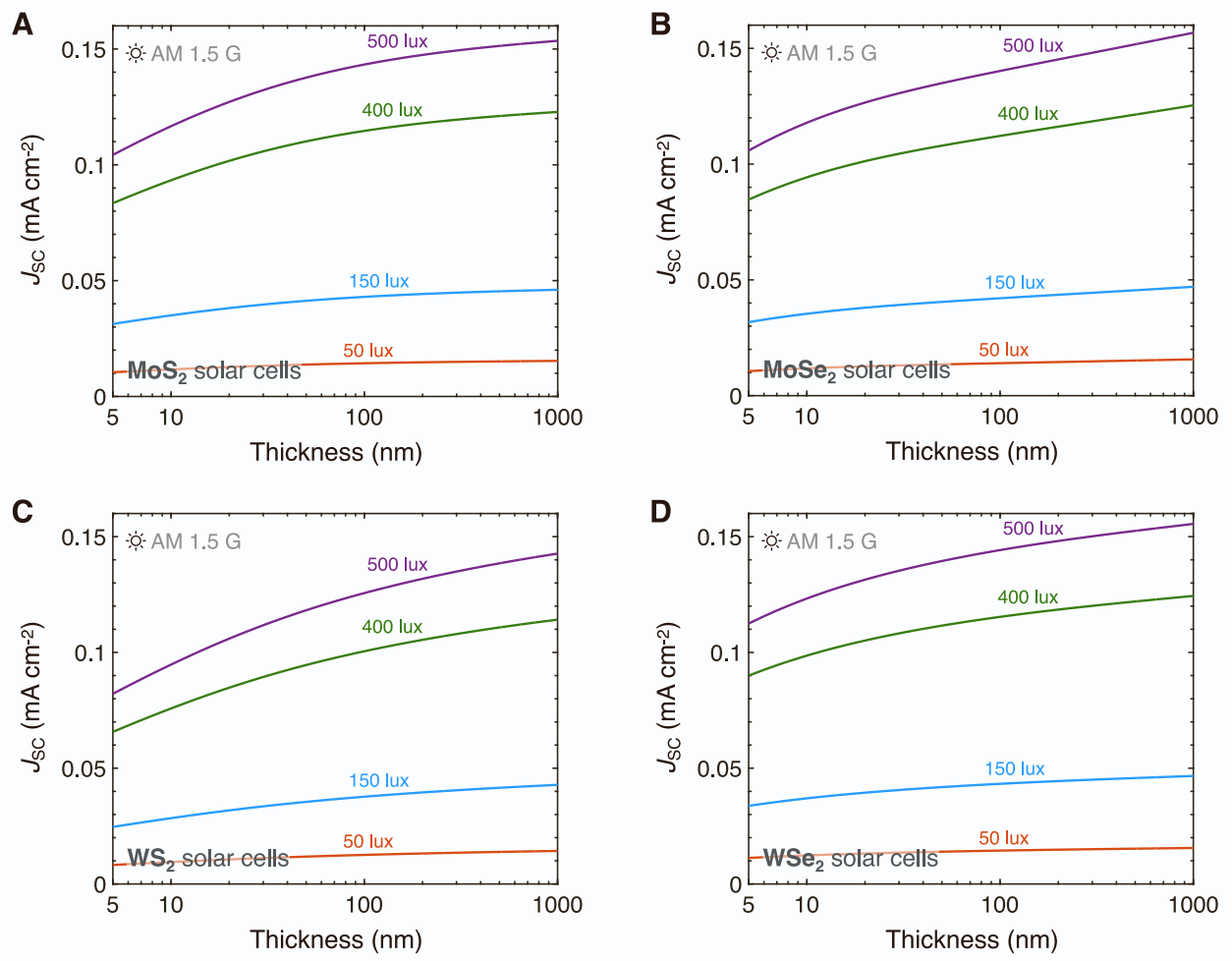

Figure S14. Short-circuit current density (J_{SC}) of thin-film TMD solar cells under AM 1.5 G illumination. J_{SC} of (A) MoS_2, (B) $MoSe_2$, (C) WS_2, and (D) WSe_2 solar cells as a function of the TMD (absorber) film thickness and AM 1.5 G illumination intensity at 300 K. Four AM 1.5 G illumination intensities correspond to the four colors, as labeled (e.g. purple is at 500 lux). The J_{SC} values under AM 1.5 G are lower than those under halogen lighting because the AM 1.5 G spectrum has a greater overlap with the CIE Photopic Luminosity Function, resulting in less photon flux for the same lux levels. This characteristic necessitates a lower AM 1.5 G illumination intensity to match the defined indoor lighting scenarios (**Table S1**), thus yielding a reduced J_{SC}.

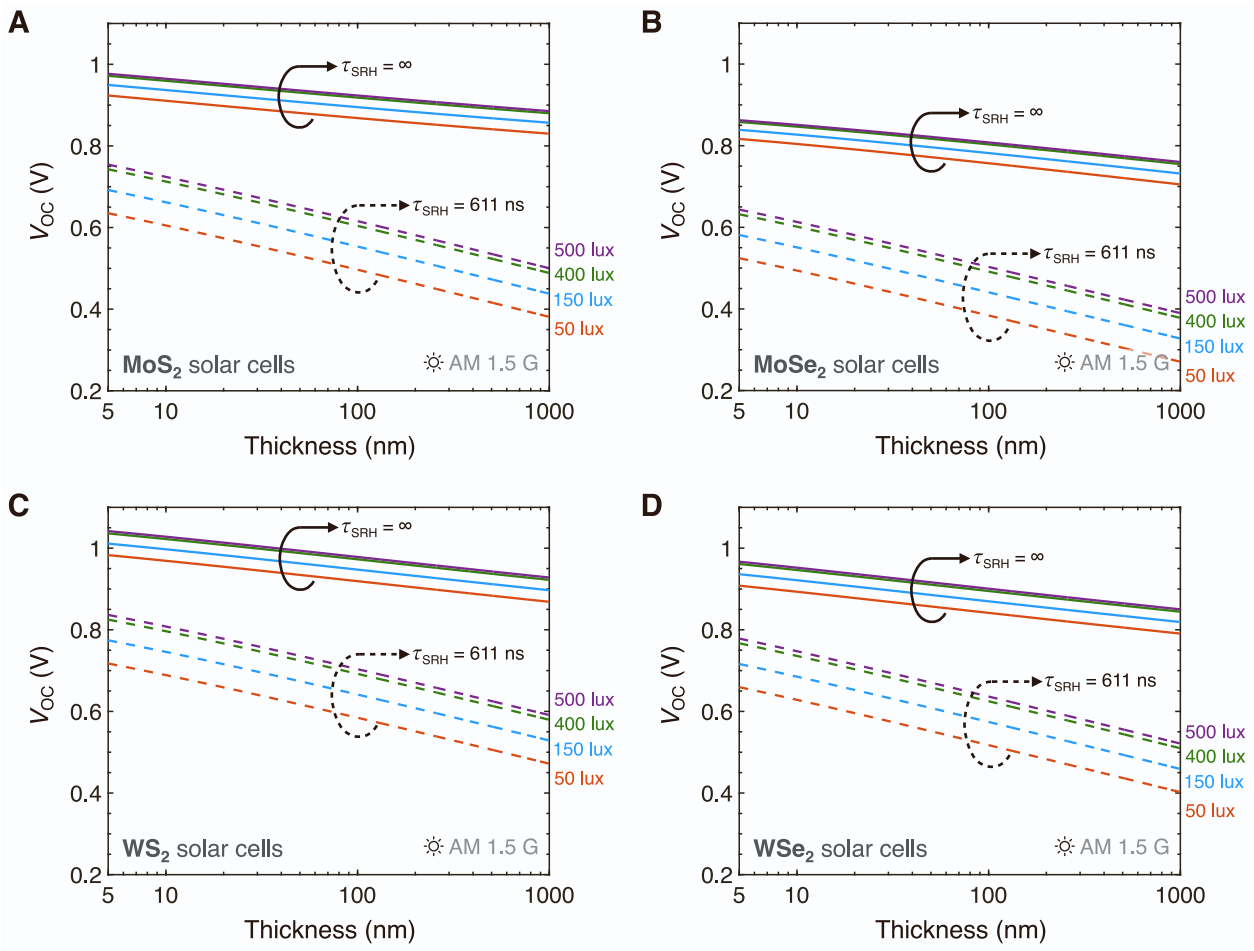

Figure S15. Open-circuit voltage (V_{OC}) of thin-film TMD solar cells under AM 1.5 G illumination. V_{OC} of (A) MoS_2, (B) $MoSe_2$, (C) WS_2, and (D) WSe_2 solar cells as a function of TMD film thickness, material quality (τ_{SRH}), and AM 1.5 G illumination intensity at 300 K. τ_{SRH}, Shockley-Read-Hall (SRH) lifetime. Solid lines are in the limit defect-free material (no SRH recombination), dashed lines with τ_{SRH} = 611 ns. Four AM 1.5 G illumination intensities correspond to the four colors, as labeled (e.g. purple dashed and solid are at 500 lux). With increasing film thickness, a noticeable decrease in V_{OC} is observed, particularly when τ_{SRH} is set at 611 ns. This decline is attributed to a shift in the absorption threshold to lower photon energies as the TMD films thicken. As a result, the effective band gap decreases, which, along with the heightened absorption of thicker films, leads to increased carrier density and a greater chance of non-radiative recombination events, thereby reducing V_{OC}.[5] The trends align with those under other illumination conditions such as CFL, LED, and halogen, where the reduction in V_{OC} is more significant with the presence of material defects as represented by the finite τ_{SRH}.

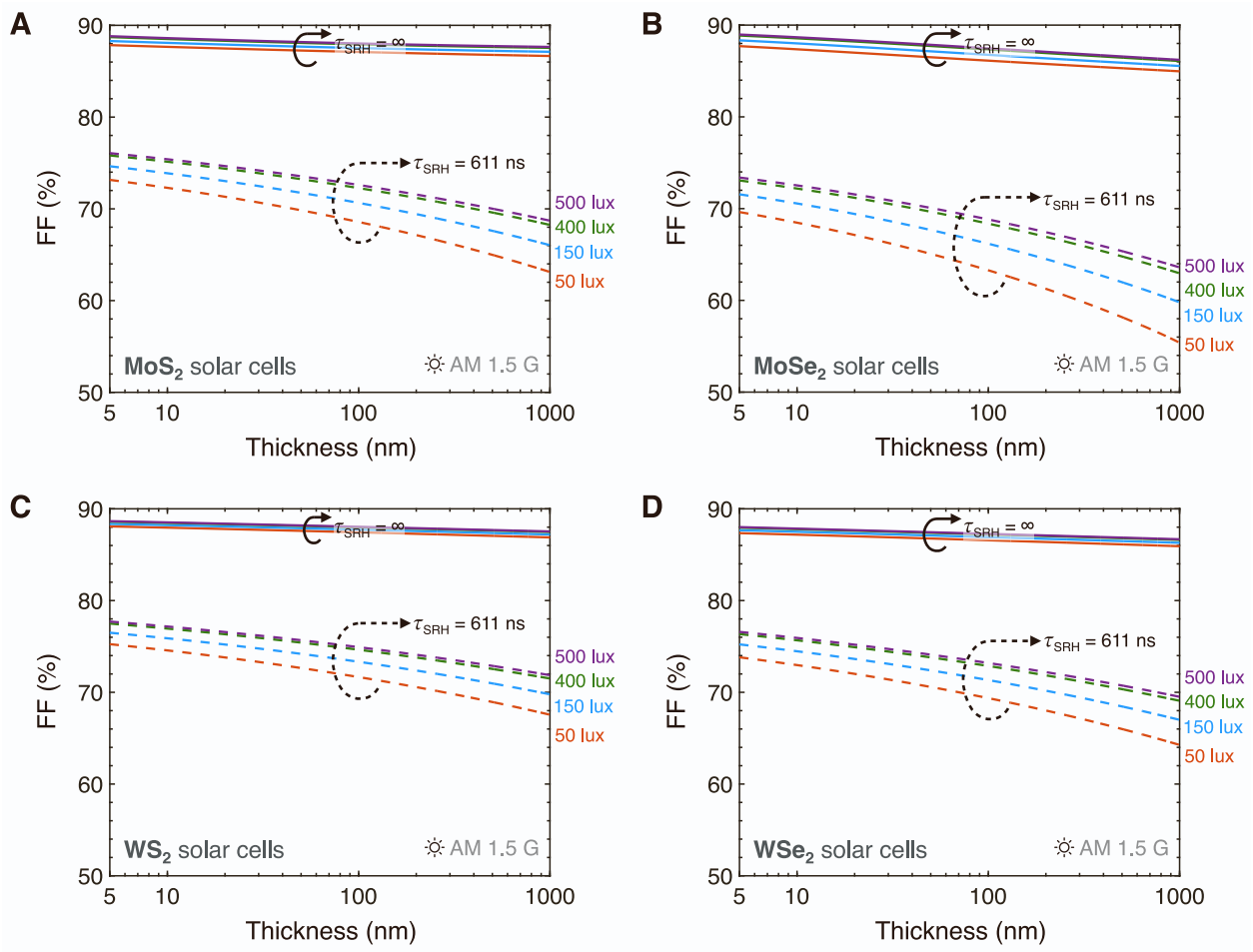

Figure S16. Fill factor (FF) of thin-film TMD solar cells under AM 1.5 G illumination. FF of (A) MoS_2, (B) $MoSe_2$, (C) WS_2, and (D) WSe_2 solar cells as a function of TMD film thickness, material quality (τ_{SRH}), and AM 1.5 G illumination intensity at 300 K. τ_{SRH}, Shockley-Read-Hall (SRH) lifetime. Solid lines are in the limit defect-free material (no SRH recombination), dashed lines with τ_{SRH} = 611 ns. Four AM 1.5 G illumination intensities correspond to the four colors, as labeled (e.g. purple dashed and solid are at 500 lux). A finite τ_{SRH} of 611 ns leads to a marked decrease in V_{OC} and thus FF with increasing film thickness. This trend largely mirrors behavior under CFL, halogen, and LED lighting, and it is consistent with the understanding that thicker films, while capturing more light, also enable more recombination events at defect sites. The FF reduction is more noticeable at higher thickness levels where defects have a greater influence on recombination. In contrast, FF remains relatively stable across various thicknesses when an infinite τ_{SRH} is assumed, indicating an ideal case with negligible defect recombination.

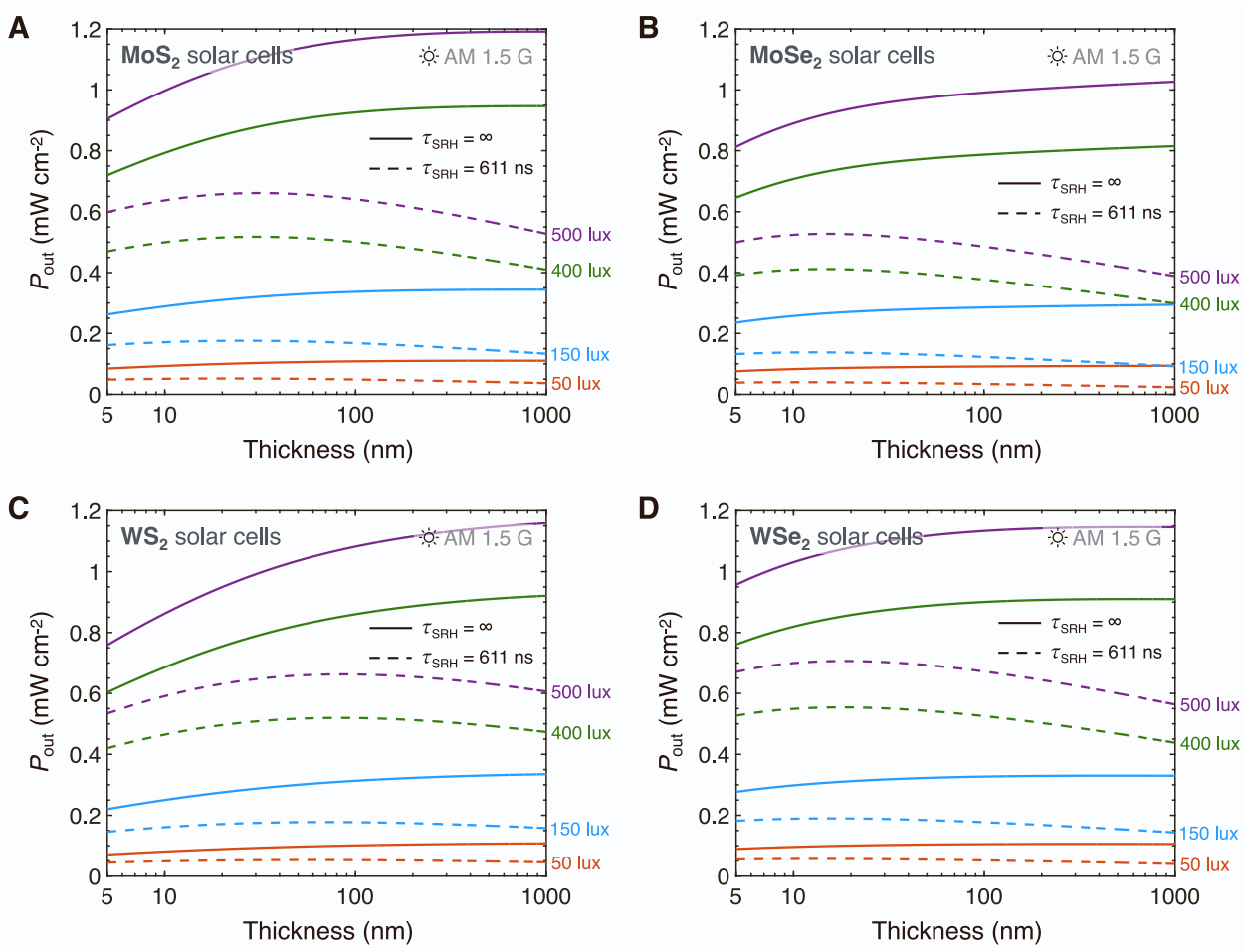

Figure S17. Output power (P_{out}) of thin-film TMD solar cells under AM 1.5 G illumination. P_{out} of (A) MoS_2, (B) $MoSe_2$, (C) WS_2, and (D) WSe_2 cells as a function of TMD film thickness, material quality (τ_{SRH}), and AM 1.5 G illumination intensity at 300 K. τ_{SRH}, Shockley-Read-Hall (SRH) lifetime. Solid lines are in the limit defect-free material (no SRH recombination), dashed lines with τ_{SRH} = 611 ns. Four AM 1.5 G illumination intensities correspond to the four colors, as labeled (e.g. purple dashed and solid are at 500 lux). Similar to halogen illumination, for an infinite SRH lifetime, P_{out} for all materials consistently rises without a peak, signifying that the positive effects of increased J_{SC} with thickness (**Figure S14**) outweigh the negative impacts on V_{OC} (**Figure S15**) and FF (**Figure S16**). However, like CFL and LED illuminations, when τ_{SRH} is finite at 611 ns, peaks in P_{out} are evident for all materials. Lower light intensities exhibit flatter peaks, as the gains in J_{SC} under these conditions fail to fully compensate for the associated losses in V_{OC} and FF.

Table 2. Literature reports on indoor photovoltaic devices. This table lists power conversion efficiencies (PCE) and associated band gaps for various indoor photovoltaic devices reported in the literature. Band gaps listed with a superscripted, bracketed reference are taken from the referenced study, otherwise they are from the source in the leftmost "Reference" column. Band gaps with an asterisk ('*') denote these were determined using the Tauc method. '**' indicates that the lux intensity of the spectrum was not specified in the reference, and no spectrum was provided, leading us to apply our spectrum to calculate the lux. Note that, even at consistent lux levels and using the same spectra, reported values vary due to differences in indoor spectra across studies.

Reference	Year	Technology	Light Source	Light Intensity (lux / μW cm^{-2})	Band Gap (eV)	PCE (%)
Kao et al.[9]	2017	Amorphous Si (a-Si:H)	CFL	500 / 162	1.70	12.69
Rossi et al.[10]	2015	Single-crystal Si (c-Si)	CFL	500 / 156.96	1.12[11]	6.11
Liu et al.[12]	2016	Dye-sensitized (DSSC)	CFL	600 / 188.1	1.66[13]	16.1
Freitag et al.[14]	2017	Dye-sensitized (DSSC)	CFL	1000 / 306.6	1.93[13]	28.9
Cao et al.[15]	2018	Dye-sensitized (DSSC)	CFL	500 / 159.1	1.50	30.8
Michaels et al.[16]	2020	Dye-sensitized (DSSC)	CFL	500 / 151.5	1.89	32.7
Zhang et al.[17]	2021	Dye-sensitized (DSSC)	CFL	500 / 159.1	1.72	32.3
Meethal et al.[18]	2023	Dye-sensitized (DSSC)	CFL	500 / 143.1	1.93[13]	30.6
Freunek et al.[19]	2013	CdTe (II-IV)	CFL	314.44** / 910	1.44	10.9
Freitag et al.[14]	2017	GaAs (III-V)	CFL	1000 / 354.0	1.42	21.0
Antunez et al.[20]	2017	CZTSSe (Kesterite)	CFL	500 / 75	1.34	11.89
Lee et al.[21]	2016	Organic	CFL	300 / 13.9	1.90	16.6
Ding et al.[22]	2019	Organic	CFL	1000 / 345	1.93	26.2
Li et al.[23]	2018	Perovskite	CFL	1000 / 278.7	1.55*	35.2

Li et al.[24]	2020	Perovskite	CFL	1000 / 286.6	1.75	32.7
Reich et al.[25]	2011	Amorphous Si (a-Si:H)	LED	1000 / 371	1.75[11]	21.0
Kim et al.[26]	2020	Amorphous Si (a-Si:H)	LED	1000 / 310	1.75[11]	29.9
Rossi et al.[10]	2015	Single-crystal Si (c-Si)	LED	500 / 164.9	1.12[11]	4.73
Liu et al.[12]	2016	Dye-sensitized (DSSC)	LED	600 / 179.2	1.66[13]	17.5
Tanaka et al.[27]	2019	Dye-sensitized (DSSC)	LED	1000 / 303.1	1.90[13]	29.2
Meethal et al.[18]	2023	Dye-sensitized (DSSC)	LED	1000 / 303.2	1.93[13]	27.1
Teran et al.[28]	2015	GaAs (III-V)	LED	580 / 159.5	1.42	19.4
Teran et al.[28]	2015	$Al_{0.2}Ga_{0.8}As$ (III-V)	LED	580 / 159.5	1.67	21.1
Ding et al.[22]	2019	Organic	LED	1000 / 360	1.93	21.7
Zhang et al.[29]	2022	Organic	LED	500 / 156	1.72	28.3
Xie et al.[30]	2023	Organic	LED	500 / 140	1.81[31]	24.94
Lee et al.[32]	2023	Organic	LED	1000 / 280	1.57	16.35
Wang et al.[33]	2023	Organic	LED	500 / 157.78	1.63*	29.0
Li et al.[24]	2020	Perovskite	LED	1000 / 279.6	1.75	35.6
He et al.[34]	2021	Perovskite	LED	824.5 / 301.6	1.59	40.1
Chen et al.[35]	2021	Perovskite	LED	1000 / 278.8	1.54	40.99
Gong et al.[36]	2022	Perovskite	LED	1000 / 325	1.53*	41.23
Liu et al.[37]	2024	Perovskite	LED	1000 / 279	1.52	41.33

SUPPLEMENTARY REFERENCES

1. Tiedje, T.O.M., Yablonovitch, E.L.I., Cody, G.D., and Brooks, B.G. (1984). Limiting efficiency of silicon solar cells. IEEE Trans Electron Devices *31*, 711–716. https://doi.org/10.1109/T-ED.1984.21594.

2. van Bommel, W. (2023). Halogen Lamp. In Encyclopedia of Color Science and Technology (Springer), pp. 865–872.

3. Rühle, K., and Kasemann, M. (2013). Approaching high efficiency wide range silicon solar cells. In 2013 IEEE 39th Photovoltaic Specialists Conference (PVSC), pp. 2651–2654. https://doi.org/10.1109/PVSC.2013.6745018.

4. Young Hugh D. and Freedman, R.A. and F.L.A. and S.F.W. 1898-1975. (2020). University physics with modern physics Fifteenth edition. (Pearson Higher Education).

5. Nassiri Nazif, K., Nitta, F.U., Daus, A., Saraswat, K.C., and Pop, E. (2023). Efficiency limit of transition metal dichalcogenide solar cells. Commun Phys *6*, 367. https://doi.org/10.1038/s42005-023-01447-y.

6. Jariwala, D., Davoyan, A.R., Tagliabue, G., Sherrott, M.C., Wong, J., and Atwater, H.A. (2016). Near-unity absorption in van der Waals semiconductors for ultrathin optoelectronics. Nano Lett *16*, 5482–5487. https://doi.org/10.1021/acs.nanolett.6b01914.

7. Huang, L., Li, G., Gurarslan, A., Yu, Y., Kirste, R., Guo, W., Zhao, J., Collazo, R., Sitar, Z., Parsons, G.N., et al. (2016). Atomically thin MoS_2 narrowband and broadband light superabsorbers. ACS Nano *10*, 7493–7499. https://doi.org/10.1021/acsnano.6b02195.

8. Green, M.A. (1981). Solar cell fill factors: General graph and empirical expressions. Solid State Electronics *24*, 788–789. https://doi.org/10.1016/0038-1101(81)90062-9.

9. Kao, M.-H., Shen, C.-H., Yu, P., Huang, W.-H., Chueh, Y.-L., and Shieh, J.-M. (2017). Low-Temperature Growth of Hydrogenated Amorphous Silicon Carbide Solar Cell by Inductively Coupled Plasma Deposition Toward High Conversion Efficiency in Indoor Lighting. Sci Rep *7*, 12706. https://doi.org/10.1038/s41598-017-10661-y.

10. De Rossi, F., Pontecorvo, T., and Brown, T.M. (2015). Characterization of photovoltaic devices for indoor light harvesting and customization of flexible dye solar cells to deliver superior efficiency under artificial lighting. Appl Energy *156*, 413–422. https://doi.org/10.1016/j.apenergy.2015.07.031.

11. Berwal, A.K., Kumari, N., Kaur, I., Kumar, S., and Haleem, A. (2016). Investigating the effect of spectral variations on the performance of monocrystalline, polycrystalline and amorphous silicon solar cells. Journal of Alternate Energy Sources and Technologies *7*, 28–36p.

12. Liu, Y.-C., Chou, H.-H., Ho, F.-Y., Wei, H.-J., Wei, T.-C., and Yeh, C.-Y. (2016). A feasible scalable porphyrin dye for dye-sensitized solar cells under one sun and dim light environments. J Mater Chem A Mater *4*, 11878–11887. https://doi.org/10.1039/C6TA04097G.

13. Aftabuzzaman, M., Sarker, S., Lu, C., and Kim, H.K. (2021). In-depth understanding of the energy loss and efficiency limit of dye-sensitized solar cells under outdoor and indoor conditions. J Mater Chem A Mater *9*, 24830–24848. https://doi.org/10.1039/D1TA03309C.

14. Freitag, M., Teuscher, J., Saygili, Y., Zhang, X., Giordano, F., Liska, P., Hua, J., Zakeeruddin, S.M., Moser, J.E., Grätzel, M., et al. (2017). Dye-sensitized solar cells for efficient power generation under ambient lighting. Nat Photonics *11*, 372–378. https://doi.org/10.1038/nphoton.2017.60.

15. Cao, Y., Liu, Y., Zakeeruddin, S.M., Hagfeldt, A., and Grätzel, M. (2018). Direct Contact of Selective Charge Extraction Layers Enables High-Efficiency Molecular Photovoltaics. Joule *2*, 1108–1117. https://doi.org/10.1016/j.joule.2018.03.017.

16. Michaels, H., Rinderle, M., Freitag, R., Benesperi, I., Edvinsson, T., Socher, R., Gagliardi, A., and Freitag, M. (2020). Dye-sensitized solar cells under ambient light powering machine learning: Towards autonomous smart sensors for the internet of things. Chem Sci *11*, 2895–2906. https://doi.org/10.1039/c9sc06145b.

17. Zhang, D., Stojanovic, M., Ren, Y., Cao, Y., Eickemeyer, F.T., Socie, E., Vlachopoulos, N., Moser, J.-E., Zakeeruddin, S.M., Hagfeldt, A., et al. (2021). A molecular photosensitizer achieves a V_{oc} of 1.24 V enabling highly efficient and stable dye-sensitized solar cells with copper(II/I)-based electrolyte. Nat Commun *12*, 1777. https://doi.org/10.1038/s41467-021-21945-3.

18. Meethal, S.M., Pradhan, S.C., Velore, J., Varughese, S., Pillai, R.S., Sauvage, F., Hagfeldt, A., and Soman, S. (2024). Asymmetric dual species copper (II/I) electrolyte dye-sensitized solar cells with 35.6% efficiency under indoor light. J Mater Chem A Mater *12*, 1081–1093. https://doi.org/10.1039/D3TA06046B.

19. Freunek, M., Freunek, M., and Reindl, L.M. (2013). Maximum efficiencies of indoor photovoltaic devices. IEEE J Photovolt *3*, 59–64. https://doi.org/10.1109/JPHOTOV.2012.2225023.

20. Antunez, P.D., Bishop, D.M., Luo, Y., and Haight, R. (2017). Efficient kesterite solar cells with high open-circuit voltage for applications in powering distributed devices. Nat Energy *2*, 884–890. https://doi.org/10.1038/s41560-017-0028-5.

21. Lee, H.K.H., Li, Z., Durrant, J.R., and Tsoi, W.C. (2016). Is organic photovoltaics promising for indoor applications? Appl Phys Lett *108*. https://doi.org/10.1063/1.4954268.

22. Ding, Z., Zhao, R., Yu, Y., and Liu, J. (2019). All-polymer indoor photovoltaics with high open-circuit voltage. J. Mater. Chem. A *7*, 26533–26539. https://doi.org/10.1039/C9TA10040G.

23. Li, M., Zhao, C., Wang, Z.-K., Zhang, C.-C., Lee, H.K.H., Pockett, A., Barbé, J., Tsoi, W.C., Yang, Y.-G., Carnie, M.J., et al. (2018). Interface modification by ionic liquid: a promising candidate for indoor light harvesting and stability improvement of planar perovskite solar cells. Adv Energy Mater *8*, 1801509. https://doi.org/10.1002/aenm.201801509.

24. Li, Z., Zhang, J., Wu, S., Deng, X., Li, F., Liu, D., Lee, C., Lin, F., Lei, D., Chueh, C.-C., et al. (2020). Minimized surface deficiency on wide-bandgap perovskite for efficient indoor photovoltaics. Nano Energy *78*, 105377. https://doi.org/10.1016/j.nanoen.2020.105377.

25. Reich, N.H., van Sark, W.G.J.H.M., and Turkenburg, W.C. (2011). Charge yield potential of indoor-operated solar cells incorporated into Product Integrated Photovoltaic (PIPV). Renew Energy *36*, 642–647. https://doi.org/10.1016/j.renene.2010.07.018.

26. Kim, G., Lim, J.W., Kim, J., Yun, S.J., and Park, M.A. (2020). Transparent Thin-Film Silicon Solar Cells for Indoor Light Harvesting with Conversion Efficiencies of 36% without Photodegradation. ACS Appl Mater Interfaces *12*, 27122–27130. https://doi.org/10.1021/acsami.0c04517.

27. Tanaka, E., Michaels, H., Freitag, M., and Robertson, N. (2020). Synergy of co-sensitizers in a copper bipyridyl redox system for efficient and cost-effective dye-sensitized solar cells in solar and ambient light. J Mater Chem A Mater *8*, 1279–1287. https://doi.org/10.1039/C9TA10779G.

28. Teran, A.S., Wong, J., Lim, W., Kim, G., Lee, Y., Blaauw, D., and Phillips, J.D. (2015). AlGaAs Photovoltaics for Indoor Energy Harvesting in mm-Scale Wireless Sensor Nodes. IEEE Trans Electron Devices *62*, 2170–2175. https://doi.org/10.1109/TED.2015.2434336.

29. Zhang, T., An, C., Xu, Y., Bi, P., Chen, Z., Wang, J., Yang, N., Yang, Y., Xu, B., Yao, H., et al. (2022). A Medium-Bandgap Nonfullerene Acceptor Enabling Organic Photovoltaic Cells with 30% Efficiency under Indoor Artificial Light. Advanced Materials *34*, 2207009. https://doi.org/10.1002/adma.202207009.

30. Bi, P., Zhang, S., Ren, J., Chen, Z., Zheng, Z., Cui, Y., Wang, J., Wang, S., Zhang, T., Li, J., et al. (2021). A high-performance nonfused wide-bandgap acceptor for versatile photovoltaic applications. Advanced Materials *34*, 2108090. https://doi.org/10.1002/adma.202108090.

31. Xie, C., Xiao, C., Fang, J., Zhao, C., and Li, W. (2023). Core/shell AgNWs@SnO_x electrodes for high performance flexible indoor organic solar cells with> 25% efficiency. Nano Energy *107*, 108153. https://doi.org/10.1016/j.nanoen.2022.108153.

32. Lee, Y., Biswas, S., Choi, H., and Kim, H. (2023). Record High Efficiency Achievement under LED Light in Low Bandgap Donor-Based Organic Solar Cell through Optimal Design. Int J Energy Res *2023*, 3823460. https://doi.org/10.1155/2023/3823460.

33. Wang, W., Cui, Y., Zhang, T., Bi, P., Wang, J., Yang, S., Wang, J., Zhang, S., and Hou, J. (2023). High-performance organic photovoltaic cells under indoor lighting enabled by suppressing energetic disorders. Joule *7*, 1067–1079. https://doi.org/10.1016/j.joule.2023.04.003.

34. He, X., Chen, J., Ren, X., Zhang, L., Liu, Y., Feng, J., Fang, J., Zhao, K., and Liu, S. (2021). 40.1% record low-light solar-cell efficiency by holistic trap-passivation using micrometer-thick perovskite film. Advanced Materials *33*, 2100770. https://doi.org/10.1002/adma.202100770.

35. Chen, C.-H., Lou, Y.-H., Wang, K.-L., Su, Z.-H., Dong, C., Chen, J., Shi, Y.-R., Gao, X.-Y., and Wang, Z.-K. (2021). Ternary two-step sequential deposition induced perovskite orientational crystallization for high-performance photovoltaic devices. Adv Energy Mater *11*, 2101538. https://doi.org/10.1002/aenm.202101538.

36. Gong, O.Y., Han, G.S., Lee, S., Seo, M.K., Sohn, C., Yoon, G.W., Jang, J., Lee, J.M., Choi, J.H., Lee, D.-K., et al. (2022). Van der Waals force-assisted heat-transfer engineering for overcoming limited efficiency of flexible perovskite solar cells. ACS Energy Lett *7*, 2893–2903. https://doi.org/10.1021/acsenergylett.2c01391.

37. Liu, C., Yang, T., Cai, W., Wang, Y., Chen, X., Wang, S., Huang, W., Du, Y., Wu, N., Wang, Z., et al. (2024). Flexible Indoor Perovskite Solar Cells by In Situ Bottom-Up Crystallization Modulation and Interfacial Passivation. Advanced Materials *36*, 2311562. https://doi.org/10.1002/adma.202311562.